https://doi.org/10.5194/essd-2023-172
Preprint. Discussion started: 17 July 2023

Open Access Earth System Science Data Discussions

Cloud condensation nuclei concentrations derived from the CAMS reanalysis

Karoline Block[1], Mahnoosh Haghighatnasab[1], Daniel Partridge[2], Philip Stier[3], and Johannes Quaas[1]

[1]Leipzig Institute for Meteorology, Faculty of Physics and Earth Sciences, University of Leipzig, Germany
[2]Department of Mathematics and Statistics, Faculty of Environment, Science and Economy, University of Exeter, Exeter, United Kingdom
[3]Atmospheric, Oceanic and Planetary Physics, Department of Physics, University of Oxford, Oxford, United Kingdom

Correspondence: Karoline Block (karoline.block@uni-leipzig.de)

Abstract. Determining concentrations of cloud condensation nuclei (CCN) is one of the first steps in the chain in analysis of cloud droplet formation, the direct microphysical link between aerosols and cloud droplets, a process key for aerosol-cloud interactions (ACI). However, due to sparse coverage of in-situ measurements and difficulties associated with retrievals from satellites, a global exploration of their magnitude, source, temporal and spatial distribution cannot be easily obtained. Thus, a better representation of CCN is one of the goals for quantifying ACI processes and achieving uncertainty reduced estimates of their associated radiative forcing.

Here, we introduce a new CCN dataset which is derived based on aerosol mass mixing ratios from the latest Copernicus Atmosphere Monitoring Service (CAMS) reanalysis (RA: EAC4) in a diagnostic model that uses CAMSRA aerosol properties and a simplified kappa-Köhler framework suitable for global models. The emitted aerosols in CAMS are not only based on input from emission inventories using aerosol observations, they also have a strong tie to satellite-retrieved aerosol optical depth (AOD) as this is assimilated as a constraining factor in the reanalysis. Furthermore, the reanalysis interpolates for cases of poor or missing retrievals and thus allows for a full spatio-temporal quantification of CCN.

This paper illustrates the temporal and spatial structure of CCN and their abundance in the atmosphere. A brief evaluation with ground based in-situ measurements demonstrates the improvement of the modeled CCN over the sole use of AOD as a proxy for CCN.

The CCN dataset, which is now freely available to users (Block, 2023), features 3-D CCN concentrations of global coverage for various supersaturations and aerosol species covering the years from 2003 to 2021 with daily frequency. This dataset is one of its kind as it offers lots of opportunities to be used for evaluation in models and in ACI studies.

1 Introduction

Processes of aerosol-cloud interactions (ACI) are still associated with large uncertainties in their contribution to climate forcing (Forster et al., 2021). One of the reasons for this is an insufficient determination of cloud condensation nuclei (CCN) concentrations which are a key element for ACI processes. A global exploration of their magnitude, source, temporal and spatial distribution is challenging for various reasons. CCN can either be directly detected by in-situ measurements (e.g. using CCN

https://doi.org/10.5194/essd-2023-172
Preprint. Discussion started: 17 July 2023

counters) or estimated from related optical properties from remote sensing observations (e.g. from AERONET photometers). However, airborne or ground-based observations provide only sparse information. For that reason observational ACI studies often rely on optical properties from satellite retrievals. The difficulty in these remote sensing applications is however the difference between the size range relevant for light extinction and the size range important for CCN concentrations (Andreae, 2009). Nevertheless, aerosol optical properties such as aerosol optical depth (AOD) are commonly used as proxies for CCN in ACI studies (e.g. Kaufman et al., 2005; Quaas et al., 2008, 2009; Grandey and Stier, 2010; Gryspeerdt and Stier, 2012; Bellouin et al., 2013; Koren et al., 2014; Bellouin et al., 2020).

Even though it has been shown that AOD is suitable as a first indicator of CCN concentrations (Andreae, 2009), it suffers from various deficiencies which make it difficult to get a correct estimate of CCN. Firstly, AOD is a column integrated property and does not provide a vertical resolution of CCN which is needed when interactions with clouds are studied (Stier, 2016; Quaas et al., 2020). Further, the variability in the scale height of the vertical aerosol distribution and the existence of aerosol layers aloft can introduce substantial variability in the relationship between column and surface properties (Jia et al., 2022). Secondly, AOD can only be retrieved in cloud-free conditions and mostly over dark surfaces, so that larger areas such as the Sahara, the poles or areas with permanent cloud cover (e.g. stratocumulus decks) are not or insufficiently covered (e.g., Jia et al., 2021). Therefore, as satellite retrieved AOD does not offer a complete temporal and spatial coverage of the Earth's surface, sampling biases are introduced in its statistics. Thirdly, AOD, and also related optical properties such as the aerosol index (AI), cannot provide a specification of the involved aerosol components which matters to determine their suitability as CCN (e.g., Hasekamp et al., 2019). Fourthly, changes in relative humidity (RH) can result in pronounced variations of AOD due to aerosol swelling effects, while the actual number of CCN remains constant (e.g., Quaas et al., 2009).

Even though various studies using AI instead of AOD found an improvement in the relationship to CCN (e.g. Nakajima et al., 2001; Kapustin et al., 2006; Liu and Li, 2014; Gryspeerdt et al., 2017), the problems listed above still remain. Stier (2016) who analysed the relationship between AOD and CCN using a fully self-consistent global model (ECHAM-HAM) found correlation coefficients between CCN at 0.2 % supersaturation and AOD to be below 0.5 for 71 %of the area of the globe, implying that AOD variability explains only 25 % of the CCN variance. Correlations with alternative aerosol radiative properties proposed as superior proxies of CCN such as fine mode aerosol optical depth, dry aerosol optical depth and aerosol index do not give significant improvements according to this study. Hasekamp et al. (2019) retrieved CCN concentrations from the polarimetric satellite POLDER-3 aerosol product and showed that there is not a simple scaling between AOD and CCN due to the impact of differing aerosol species. Furthermore, they demonstrated that the radiative forcing from ACIs is significantly underestimated when AOD or AI are used as CCN proxies. Shinozuka et al. (2015) have examined the relationship between CCN and dry extinction for a variety of airborne and ground-based observations. They also demonstrated that the uncertainty in the CCN-AOD relationship arises not only from the uncertainty in the relationship between CCN and dry extinction, but also from the humidity response of light extinction, the vertical profile, the horizontal-temporal variability and the AOD measurement error. These examples illustrate how important it is to account for the uncertainties related with CCN proxies and show the need for new strategies.

https://doi.org/10.5194/essd-2023-172
Preprint. Discussion started: 17 July 2023

Several attempts exist to provide a more comprehensive picture on CCN related aerosol properties. Kinne et al. (2013) introduced the MAC-v1 climatology for tropospheric aerosol, which describes optical properties such as AOD, SSA (single scattering albedo) and fine-mode AOD fraction of tropospheric aerosols on monthly timescales and with global coverage. Aerosol mass concentrations from 24 European sites produced by various institutes using different techniques have been comprehensively assessed in a European aerosol phenomenology, which analyses PM10 and PM2.5 mass concentrations, their chemical composition and aerosol particle size distributions (Van Dingenen et al., 2004; Putaud et al., 2004, 2010). Asmi et al. (2011) have analysed two years of harmonized aerosol number size distribution data from 24 European field monitoring sites, focusing on near surface aerosol particle number concentrations and number size distributions between 30 and 500 nm of dry particle diameter, that is relevant for CCN sized aerosols. Winker et al. (2013) focused more on the aerosol vertical distribution, by constructing a monthly global gridded dataset of daytime and nighttime aerosol extinction profiles from Caliop lidar observations, thus introducing an initial global 3-D aerosol climatology. CALIPSO lidar retrievals also have been used by Choudhury and Tesche (2022) who derived CCN concentrations using an algorithm that relies on the optical modelling of CALIPSO aerosol microphysics. They even account for hygroscopicities and size distributions of five aerosol subtypes. A first validation of this CCN product with in-situ measurements illustrates the potential of CALIPSO for constructing a global height-resolved CCN climatology.

A synthesis of in-situ CCN measurements is provided by Spracklen et al. (2011), who used observations reported in published literature to produce a worldwide dataset of CCN, which is combined with the global model of aerosol processes (GLOMAP Spracklen et al., 2005) to explore the contribution of carbonaceous combustion aerosol to CCN. Another CCN synthesis is provided by Paramonov et al. (2015), who used measurements from the European Integrated project on Aerosol Cloud Climate and Air Quality interactions framework (EUCAARI) to analyse CCN activation and hygroscopic properties of the atmospheric aerosols. Schmale et al. (2017, 2018) have produced a harmonized dataset of long-term CCN number concentrations, particle number size distributions and chemical composition from observatories located in different environments worldwide, thus presenting yet another CCN synthesis.

All of these studies taken together provide a sound foundation of CCN relevant aerosol properties, but most of them do not refer to actual CCN concentrations at specific supersaturations but rather to proxies such as absorption or scattering coefficients or aerosol numbers integrated over a certain size range, e.g. N_{100} referring to particles with diameters above 100 nm as being relevant for activation. The ones who do measure actual CCN concentrations (CCN syntheses) usually don't give a global coverage nor a vertically resolved picture. Furthermore, it is challenging to use such syntheses e.g. for evaluation of GCMs as they are produced by different instruments which report at different supersaturation bands and involve different measurement uncertainties.

In this study we suggest a new approach to resolve these issues by computing CCN from an aerosol reanalysis provided by the European Centre for Medium-range Weather Forecast (ECMWF). In contrast to satellite retrievals, the atmospheric model including aerosol and chemistry modules (here, ECMWF IFS) can simulate the full spatial and temporal distributions of aerosols. Deviations to real aerosol distributions and life cycles are reduced by constraining modelled estimates with observations (Kapsomenakis et al., 2022). This is done in the Copernicus Atmosphere Monitoring Service (CAMS) reanalysis

https://doi.org/10.5194/essd-2023-172
Preprint. Discussion started: 17 July 2023

(Inness et al., 2019b), in which assimilated AOD from the Moderate Resolution Imaging Spectroradiometer (MODIS, Levy et al., 2013) is used to constrain the bulk total aerosol mass mixing ratio modelled with the IFS. Thus, a strong relationship between observation and model is kept, while additional information on the vertical distribution, the horizontal and temporal coverage, the aerosol speciation and hygroscopic effects is provided by the model.

2 The CCN climatology computed from CAMS: Data provenance and structure

2.1 The CAMS model and assimilation system

The CAMS reanalysis (CAMSRA, Inness et al., 2019b) is the latest global aerosol reanalysis produced by the European Centre for Medium-range Weather Forecast (ECMWF) within the framework of the European Copernicus program to provide information on aerosols, trace and greenhouse gases in the context of operational numerical weather prediction. It is based on the Integrated Forecasting System (IFS) which has been extended by an aerosol scheme which mainly follows the aerosol treatment in the french LMD-Z model (Boucher et al., 2002; Reddy et al., 2005) and was further modified by ECMWF during the GEMS and MACC projects. This reanalysis profits from continuing upgrades in the modeling and assimilation system (see Inness et al. (2019b) and therefore shows a smaller bias compared to observed AOD than the previous reanalyses.

2.1.1 Aerosol treatment in the ECMWF IFS

CAMSRA was produced using the IFS (cycle 42r1) (Morcrette et al., 2009; Rémy et al., 2019) including a fully integrated four-dimensional assimilation apparatus employed operationally at ECMWF (Benedetti et al., 2009). Details of the aerosol and chemistry modules applied in CAMSRA can be found in Inness et al. (2019b) and Flemming et al. (2015).

The aerosol model uses a hybrid 1-moment bin-bulk scheme with 12 prognostic tracers which consist of 11 aerosol tracers and one tracer for gas-phase sulfur dioxide (SO_2) precursor. These tracers are transported by the IFS vertical diffusion and convection schemes and are advected by the semi-Lagrangian scheme. The simulated aerosol tracers are mass mixing ratios of five aerosol species which are sulfate aerosol (SU), hydrophilic and hydrophobic black carbon (BC), hydrophilic and hydrophobic organic matter (OM), as well as mineral dust (DU) and sea salt (SS) each with three size dependent bins. The limits of the three different size classes are chosen so that roughly 10, 20 and 70 % of the total mass of each aerosol type are in the various bins. Hydrophilic and hydrophobic components are prescribed via explicit emission fractions and ageing factors. The different aerosol species are assumed to be externally mixed, meaning that the individual species are assumed to coexist in the volume of air considered and to retain their individual optical and chemical characteristics, making it easier to trace them as they undergo model dynamics.

Mineral dust and sea salt emissions are parameterised using near-surface wind speeds. Sea-salt production is calculated assuming an 80 % relative humidity, but only the dry mass is added to the respective bin and transported, thus no water is transported via the aerosol and the mass is also not transferred between bins because of growth. However, wet density and

https://doi.org/10.5194/essd-2023-172
Preprint. Discussion started: 17 July 2023

radius are considered for all the size bins when dealing with dry deposition, sedimentation and radiation (Morcrette et al., 2009). DU does not experience any aging or choating and is treated entirely as an insoluble aerosol.

Near real-time fire emissions from the Global Fire Assimilation System GFASv1.2 (Kaiser et al., 2012) are used to constrain black carbon emissions from wildfires and biomass burning (Kapsomenakis et al., 2022). Freshly emitted BC is partitioned into 80 % hydrophobic and 20 % hydrophilic (Morcrette et al., 2009), while the partitioning of OM is set to 16 % hydrophobic and 84 % hydrophilic (Bozzo et al., 2020). This setup provides optical properties representing an average of biomass and anthropogenic organic carbon aerosols (Bozzo et al., 2020). Once emitted, both species experience ageing from hydrophobic to hydrophilic with a time constant of 1.16 days (Morcrette et al., 2009).

The sulfate type represents aerosols originating from sulfur emissions from industrial and fossil fuel combustion, biomass burning and natural volcanic and biogenic sources (Bozzo et al., 2020). The sulfur cycle is represented with sulfur dioxide (SO_2) produced at or near the surface which is being transformed into sulfate aerosol (SO_4, or SU) using temperature, relative humidity and a prescribed, latitude dependent e-folding time scale. It should be noted here that SU emissions originating from volcanic activities do actually represent a rather continuous background source of outgassing volcanoes rather than explicit volcanic eruptions. It is further stated by Inness et al. (2019b) and Kapsomenakis et al. (2022) that there are some hotspots of increased AOD bias around outgassing volcanoes, in particular around Mauna Loa and Altzomoni near Mexico City. This might result from erroneous model treatment of diffuse volcanic emissions which enhance SU at these locations. Therefore, we follow their recommendation to exclude these two sites as unrepresentative in our analysis presented in this paper. However, in the published dataset all data are included as is.

Additionally to the emission of aerosols, CAMS includes emissions of precursors such as natural emissions for nitrogen dioxide (NO_2), dimethyl sulfate (DMS) and, as already stated above, sulfur dioxide (SO_2). Biogenic emissions are done as monthly means for volatile organic compounds (VOC) which are calculated offline by the MEGAN2.1 model (Guenther et al., 2006) using MERRA-2 reanalysed meteorology following Sindelarova et al. (2014). Anthropogenic emissions from the MACCity inventory (Granier et al., 2011), including an upgrade for CO emissions (Stein et al., 2014), covers the period 1960–2010 and is updated for subsequent years using the representative concentration pathway (RCP) version 8.5, the "business-as-usual" scenario. Anthropogenic secondary organic aerosol (SOA) production has also been implemented in CAMS, proportional to MACCity CO emissions as suggested by Spracklen et al. (2011). However, nitrate aerosols are not yet included in the aerosol scheme. The missing nitrate is likely to cause an underestimation of total aerosol in the forecast model in regions where nitrate would be a significant component, however in the reanalysis the total aerosol is corrected by the assimilation of total AOD observations (Inness et al., 2019b). Further it should be noted that only aerosol emissions from the surface and within the troposphere are considered in the model, a stratospheric contribution is not included.

The removal of aerosols is modelled by several processes: by dry deposition including the turbulent transfer to the surface and gravitational settling, or by wet deposition including rainout and washout of aerosol particles in and below the clouds. Wet deposition is modelled separately for convective and large-scale precipitation. The fraction of aerosol included in droplets through dissolution or impaction is set to 0.7 for all CCN relevant aerosol species (Morcrette et al., 2009).

https://doi.org/10.5194/essd-2023-172
Preprint. Discussion started: 17 July 2023

2.1.2 Aerosol confinement by assimilated AOD

The IFS assimilation apparatus has been extended to include atmospheric tracers among the control variables. A control variable is used to optimize the cost function which measures the distance between observations and their model equivalent. It is minimized in a variational assimilation approach which is described by Benedetti et al. (2009).

The observation relevant to constrain aerosol mass is the AOD. More specifically, it is the dark target AOD at 0.55 μm from the MODerate resolution Imaging Spectroradiometer (MODIS collection 6 on board of the Aqua and Terra satellites, Remer et al., 2005; Levy et al., 2013, 2018), along with the Advanced Along-Track Scanning Radiometer (AATSR) AOD onboard of the ENVISAT satellite (Popp et al., 2016) which are assimilated in the IFS. However, AOD is not retrieved in pixels identified as cloudy, nor at high latitudes where the solar illumination is small (thus assimilation is limited to the regions between 70° S and 70° N), nor over bright surfaces (snow covered high latitudes or the desert areas of Sahara and Australia) due to the impact of the surface reflectance on retrieval accuracy. Other factors affecting accuracy such as cloud contamination, assumptions about the aerosol types and size distribution, near-surface wind speed, radiative transfer biases, and instrumental uncertainties are also taken into account (Benedetti et al., 2009) and were reviewed previously by Zhang and Reid (2006).

For the calculation of the model equivalent AOD, the relative humidity is first computed from the model temperature, pressure and specific humidity. The appropriate mass extinction coefficients are then retrieved from a look-up table for the wavelength of interest (here, 550 nm), multiplied by the vertically integrated aerosol mass at the corresponding observation location. The total AOD τ at the respective wavelength λ is then calculated as the sum of the single-species AODs (Benedetti et al., 2009).

Total and component AODs are diagnosed at 17 MODIS correspondent wavelengths ranging from 0.34 to 2.13 μm by using precomputed optical properties, such as mass extinction coefficient α_e, single scattering albedo ω, and asymmetry parameter ϱ (Morcrette et al., 2009). The optical characteristics of the aerosols are computed using Mie theory (Ackerman and Toon, 1981), and are then integrated over the physical size range using the model's prescribed lognormal distributions which are fixed for each tracer (Benedetti et al., 2009). Sea salt and dust AODs are obtained by summing over the individual bin contributions. Optical properties of hygroscopic aerosols are parameterized as a function of relative humidity accounting for the respective growth factors listed by Bozzo et al. (2020).

The model control variable which is modified according to the outcome of the data assimilation, is the total aerosol mass mixing ratio, defined as the sum of all aerosol species. At each iteration of the minimization, the increments in the total mass mixing ratio derived from the assimilation of MODIS AOD have to be redistributed into the mixing ratios of the single species. Thereby each aerosol component is corrected in proportion of its original contribution to the total aerosol mass, meaning that the modelled speciation is not changed by the assimilation. It should be noted here that the assimilation modifies the modelled field not only at the point of observation but also around it. Regions with no observations because of cloudiness or high surface reflectance will still be improved by the data assimilation, but to a lesser extent than regions closer to the location of assimilated data (Benedetti et al., 2009).

https://doi.org/10.5194/essd-2023-172
Preprint. Discussion started: 17 July 2023

2.2 Computation of CCN with a modified kappa-Köhler approach

Using the CAMS reanalysis data (CAMSRA: Inness et al., 2019a), we have so far produced a 19 year long global CCN climatology (Block, 2023) available from 2003 to 2021 as daily averages on a Gaussian grid at a resolution of $0.75° \times 0.75°$ (T255) and 60 vertical levels, corresponding to the grid in the reanalysis. Apart from the CAMSRA data, which is available every 3 hours, CCN are currently only computed once a day at 00:00 UTC. The data comprises 3-D fields of total CCN computed for six different supersaturations (s: 0.1, 0.2, 0.4, 0.6, 0.8 and 1 %) and 3-D CCN fields containing CCN from SU, BC, OM and three size bins of SS computed for two supersaturations (s: 0.02 % and 0.8 %) comprising additional aerosol information in the lower and upper supersaturation range, respectively. The current choice of data frequency, resolution and variable dependencies such as supersaturation is made regarding general interest and suitability as well as file size, data storage and computational costs. This dataset is publicly available and offers the opportunity to be used for evaluation of GCMs/ESMs and in studies of aerosol-cloud interactions.

The CCN are calculated diagnostically in a box model, which once was created to be used for HadGEM3-UKCA (Davies et al., 2005; Mann et al., 2010; Hewitt et al., 2011; O'Connor et al., 2014; West et al., 2014), which was modified so that it also uses modules from a ECHAM5-HAM (Stier et al., 2005) and with updates to the ECHAM6 version (Stevens et al., 2013).

The model reads temperature, pressure, specific humidity and aerosol mass mixing ratios from the CAMS reanalysis. From the aerosol particle mass mixing ratio, q_p and air density, ρ_a, the particle mass concentration per volume is computed, $\rho_p = q_p \rho_a$, and from this the mass per aerosol particle m_p is computed as

$$m_p = \frac{4}{3}\pi\,\rho_p\,(r_0\beta)^3 \;\text{ with }\; \beta = \exp(1.5 \cdot \ln^2 \sigma_g), \tag{1}$$

using the Hatch-Choate conversion (Hinds, 1998) which relates the count median radius r_0 to the mass-averaged radius for the prescribed lognormal size distribution with geometric standard deviation σ_g.

The total aerosol number concentration N_a is then obtained by dividing ρ_p by the mass per aerosol particle. The resulting lognormal number distribution for an aerosol species k can be written as

$$N_{a,k}(r) = N_{a,k} \cdot \frac{1}{\sqrt{2\pi} \cdot \ln \sigma_{g,k}} \cdot \exp\left[-\frac{\ln^2(r/r_{0,k})}{2\ln^2 \sigma_{g,k}}\right]. \tag{2}$$

In order to stay consistent with the IFS model, we have chosen to use the given size distribution parameters used by the IFS to convert between aerosol optical properties and AODs (Benedetti et al., 2009). That way, the proportionality between AOD and the resulting CCN is kept. Any improvement the resulting CCN might reveal over AOD can then only arise from the vertical distribution and the simulated species contribution. The relevant parameters of the size distribution and aerosol properties used are listed in Table 1. Please note that only hydrophilic aerosol species are used for further processing. Even though the total aerosol number concentration is computed with all 11 aerosol tracers, CCN concentrations result only from hydrophilic BC and OM components in addition to SU and SS.

https://doi.org/10.5194/essd-2023-172
Preprint. Discussion started: 17 July 2023

Table 1. Hydrophilic aerosol properties used in this study for CCN computation. Size distribution properties are from Bozzo et al. (2020), and references therein. Given are the size bins of sphere radii [μm], the count median radii r_0 [μm], the geometric standard deviations σ_g and the dry aerosol densities ρ_p [g/cm^3] which are used for the lognormal size distributions. Values are for the dry aerosol a part from sea salt which is given at 80% RH. Kappa values are taken from ECHAM-HAM2 (Zhang et al., 2012) in reference to Petters and Kreidenweis (2007), with changes for sea salt according to Zieger et al. (2017).

aerosol	size bin [μm]	r_0 [μm]	σ_g	ρ_p [g/cm^3]	κ
SS small	0.03 - 0.5	0.1992	1.9	1.183	1.1
SS medium	0.5 - 5.0	1.992	2.0	1.183	1.1
SS large	5.0 - 20	1.992	2.0	1.183	1.1
OM	0.005 - 20	0.0212	2.24	1.8	0.06
BC	0.005 - 0.5	0.0118	2.0	1.0	0.06
SU	0.005 - 20	0.0355	2.0	1.76	0.6

Once the number concentration is computed for each aerosol species, we apply a modified kappa-Köhler theory to compute how many aerosols act as CCN at a specific supersaturation. Even though Köhler models with increased complexity are available (e.g. Lowe et al. (2016) or developments summarized in Kreidenweis et al. (2019)) to account for various deficiencies in the traditional Köhler theory (Köhler, 1936), we have chosen a rather simplified version to be consistent with the representation of Köhler theory in general circulation model (GCM) and Earth System Model (ESM) which need to be computationally feasible.

In the kappa-Köhler theory from Petters and Kreidenweis (2007), the relationship between the particle dry diameter D_d and CCN activity or hygroscopicity is derived using a single hygroscopicity parameter κ which represents a quantitative measure of aerosol water uptake characteristics and CCN activity. Values of κ for specific compounds, or for arbitrary mixtures, were determined experimentally by fitting CCN activity or hygroscopic growth factor data. κ values used in this study are taken from the literature and are listed in Table 1. Since we deal with external mixtures, each aerosol species has its own κ value.

Following Petters and Kreidenweis (2007), the saturation ratio S of a droplet with wet diameter D_w can be described as

$$S(D_w) = \frac{D_w^3 - {D_d}^3}{D_w^3 - {D_d}^3(1-\kappa)} \cdot \exp\left(\frac{4\sigma_{w/a} M_w}{RT\rho_w D_w}\right) \tag{3}$$

with the surface tension parameter $\sigma_{w/a}$, the universal gas constant R, temperature T, the molar mass of water M_w and the water density ρ_w. This relation is valid over the entire range of relative humidity and solution hygroscopicity (Petters and Kreidenweis, 2007). The first term is the solute term, describing the reduction of the water equilibrium vapor pressure over the solution in comparison to that over pure water and is described by Raoult's law. The second term is the curvature term described by the Kelvin equation which relates the equilibrium water vapor pressure over a pure water droplet of diameter D_w to the equilibrium vapor pressure over a flat surface at the same temperature (Seinfeld and Pandis, 2006).

https://doi.org/10.5194/essd-2023-172
Preprint. Discussion started: 17 July 2023

We now modify this relation as in Pöhlker et al. (2023) by considering only slightly supersaturated conditions such as in warm clouds, typically with supersaturations $0.1\% < s < 1.5\%$ (Spracklen et al., 2011). Assuming supersaturation $s \ll 1$ we can approximate $\ln S = \ln(1+s) \approx s$, and with assuming $D_d \ll D_w$, Eq. 3 becomes

$$\ln S \approx s = \frac{A}{D_w} - \kappa \frac{{D_d}^3}{D_w^3} \quad \text{with} \quad A = \frac{4\sigma_{\mathrm{w/a}} M_w}{RT\rho_w} \ . \tag{4}$$

This simplifies the original kappa-Köhler framework because it is not necessary to compute a hygroscopic diameter growth factor to account for the difference of $D_w - D_d$. For detailed derivation and comparison to the original Köhler equation (Köhler, 1936), please see Appendix A.

For any aerosol of dry diameter D_d, we can find the maximum $(dlnS/dD_w = ds/dD_w = 0)$ at a critical wet diameter $D_{c,w}$ of

$$D_{c,w} = \sqrt{\frac{3\kappa D_d^3}{A}} \tag{5}$$

which marks the onset of cloud drop formation. Inserting $D_{c,w}$ for D_w in Eq. 4, the corresponding critical supersaturation s_c is

$$\ln S_c \approx s_c = \sqrt{\frac{4A^3}{27\kappa D_d^3}} = \frac{2}{\sqrt{\kappa}} \left(\frac{A}{3D_d}\right)^{\frac{3}{2}} \quad \text{or with setting} \ \ D_d = 2r_d \ , \tag{6}$$

$$\ln S_c \approx s_c = \frac{2}{\sqrt{\kappa}} \left(\frac{A_r}{3r_d}\right)^{\frac{3}{2}} \quad \text{with} \quad A_r = \frac{2\sigma_{\mathrm{w/a}} M_w}{RT\rho_w} \ . \tag{7}$$

The critical supersaturation of the smallest aerosol particle in an aerosol population being activated is equal to the ambient or maximum supersaturation s_{max} of an air parcel rising adiabatically at uniform speed (Abdul-Razzak et al., 1998). Its critical dry radius $r_{c,d}$ is then related to s_{max} as

$$s_{\text{max}} = \frac{2}{\sqrt{\kappa}} \cdot \left(\frac{A_r}{3r_{c,d}}\right)^{\frac{3}{2}} \ . \tag{8}$$

Particles smaller than $r_{c,d}$ require a higher s_c than s_{max} and are not activated. Particles larger than $r_{c,d}$ require a smaller s_c than s_{max} and activate to form cloud droplets. Thus, CCN can be described as potential cloud droplet numbers (CDNC) as they are computed at a given supersaturation, meaning the ambient or maximum supersaturation is prescribed. For a given set of s_{max}, as we prescribe them in this dataset, the corresponding dry critical radii is computed by inverting Eq. 8.

The number concentration of activated aerosols is the number concentration of aerosols larger than the size of the smallest activated aerosol, thus with a dry critical radius of $r_{c,d}$. The calculation of the activated number fraction from the dry critical

https://doi.org/10.5194/essd-2023-172
Preprint. Discussion started: 17 July 2023

radii is done by transforming the individual log-normal distributions to an error function (Ghan et al., 1993; Khvorostyanov and Curry, 2006) which is then computed cumulatively following (Vignati et al., 2004).

3 Results and Discussion

3.1 Total CCN concentration derived from CAMS

Figure 1 shows the global distribution of total CCN load [m^{-2}] for different values of supersaturations over the troposphere, as well as the vertical distribution of zonal mean CCN concentrations [cm^{-3}]. The CCN load is determined by the emission rate, the scavenging rate and advection. Overall, the industrial and developing countries in the northern hemisphere show high CCN loads, which are maximum at a latitude of $\sim 30°$ N, originating especially from polluted regions over South-East Asia, with peaks over China and northern India. Polluted regions in the southern hemisphere, especially those in South America (Brazil's Amazon Rainforest) and Africa (Congo Basin), become better visible with larger supersaturations.
CCN concentrations decrease towards the poles where aerosol emission or advection is reduced. Regions with especially low aerosol loads apart from the poles are western Australia, the Weddel Sea and Greenland. Only a slight reduction of CCN by scavenging (Figure 1, right panels) can be found for this annual average in the inter-tropical convergence zone (ITCZ) which is determined by convective precipitation. The vertical distribution reveals that CCN concentration stay mostly in the boundary layer and decrease with height. The larger the supersaturation becomes the more CCN are available in higher altitudes. This agrees with findings of Watson-Parris et al. (2019) who analyzed the vertical distribution of global aerosol with in situ aircraft measurements. Furthermore, it can be seen that the Arctic is much more connected to NH aerosol emissions, while the Antarctic shows concentrations which are decoupled from SH emissions and advections, which is due to the West Wind Drift.

Figure 2 shows the zonal and meridional means of seasonally averaged CCN load at 0.2 % supersaturation. The seasonal, longitudinal and latitudinal variation would have been similar with other chosen values of supersaturations. The total CCN load clearly shows a seasonal cycle, with larger loads during spring and summer within the respective hemisphere. This originates mostly from natural seasonal variations in OM. However, the seasonal variability is not all naturally driven, but also anthropogenically. The meridional mean CCN load reveals a strong contribution from SU leading to high aerosol concentrations over China ($\sim 120°$ E) all year long. Otherwise, we can find the seasonal variation from the top panel being reflected in the bottom panel, with higher concentrations in spring and summer originating from the OM variations over the NH landmasses. Especially low aerosol concentrations and only little seasonal dependence can be found over the East Pacific ($\sim 40°$ W).

Figure 3 shows the anomalies of total CCN load at 0.2 % supersaturation for different bands of latitudes. It reveals specific events when the CCN load was particularly high or low compared to the multi-year monthly mean. We have identified three of these spikes (numbered in grey) to show (1) the severe Siberian Taiga Fires in Russia in 2003, (2) the 2020 Australian Bushfires and (3) the very low CCN concentrations (especially in NH) during the summer months in 2020 and 2021, which where in parts associated with the COVID-19 confinements in countries all over the world. These low CCN events alternate with events of high CCN abundance due to the wildfires in California in 2020 and in British Columbia in 2021. We can see

https://doi.org/10.5194/essd-2023-172
Preprint. Discussion started: 17 July 2023

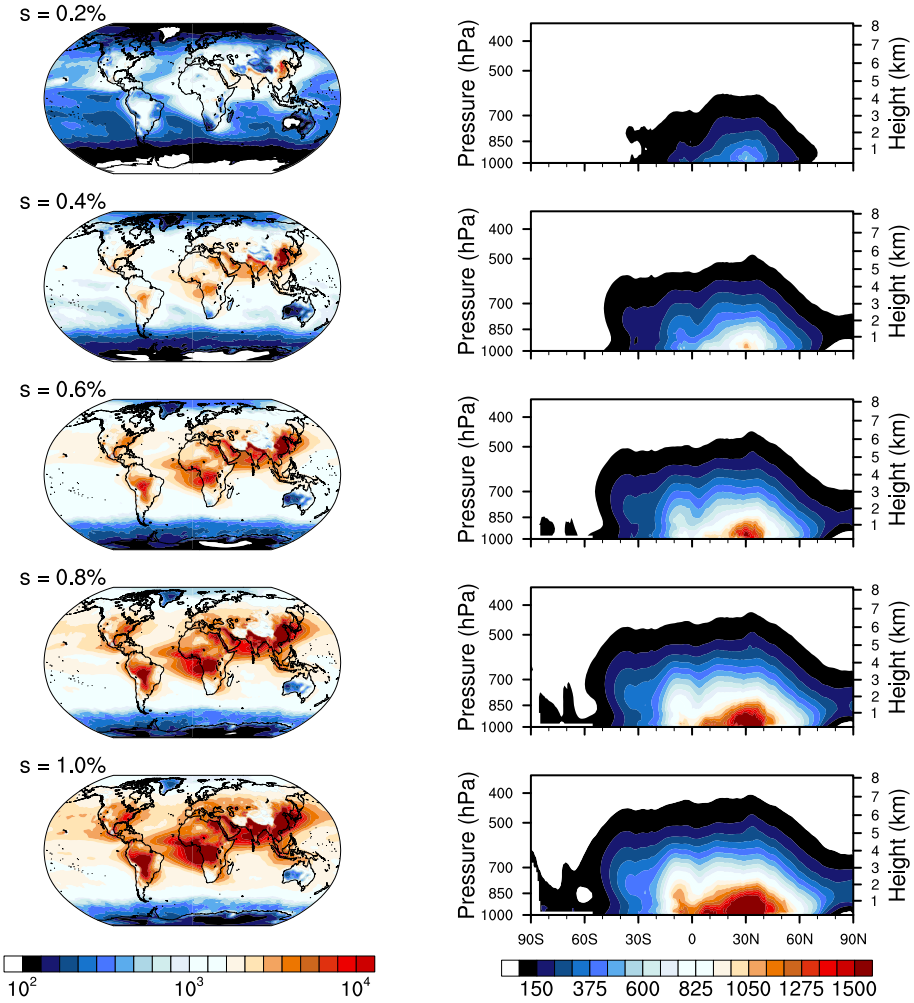

Figure 1. CCN load [$\times 10^9$ m^{-2}] of the lowermost 10 km (left panel) and corresponding zonal mean CCN concentration over height [cm^{-3}] (right panel) for supersaturations ranging from s = 0.2 % (top) to s = 1.0 % (bottom). CCN are averaged in time for the year 2007, with Mauna Loa and Mexico City being excluded. Please note that the color scale for the left panel is logarithmic while it is not for the right panel.

here that wildfires and biomass burning events show a major contribution to total CCN and that these events are well captured by the CAMS assimilation. In contrast, volcanic eruptions, e.g. the Holuhraun eruption on Iceland in 2014 (Haghighatnasab et al., 2022; Malavelle et al., 2017), have not been captured by the CAMS assimilation system nor are they modelled by the IFS as plume injections of aerosols and therefore they cannot be found in CCN load anomalies. Furthermore, we find that the time evolution of global mean CCN abundance (not plotted here) shows a significant negative trend, for s = 0.2 % it is $\approx -3 \cdot 10^9$ CCN m^{-2}year^{-1} (on 95 % significance level), which originates from latitudes between 30° N and 60° N (here the trend is $\approx -12 \cdot 10^9$ CCN m^{-2}year^{-1} for s = 0.2 %), while other latitudes do not show significant trends. This is reflected in trends of CCN load anomalies. The magnitude and/or occurrence of positive anomalies in the $30° - 60°$ N latitudinal band tend

https://doi.org/10.5194/essd-2023-172
Preprint. Discussion started: 17 July 2023

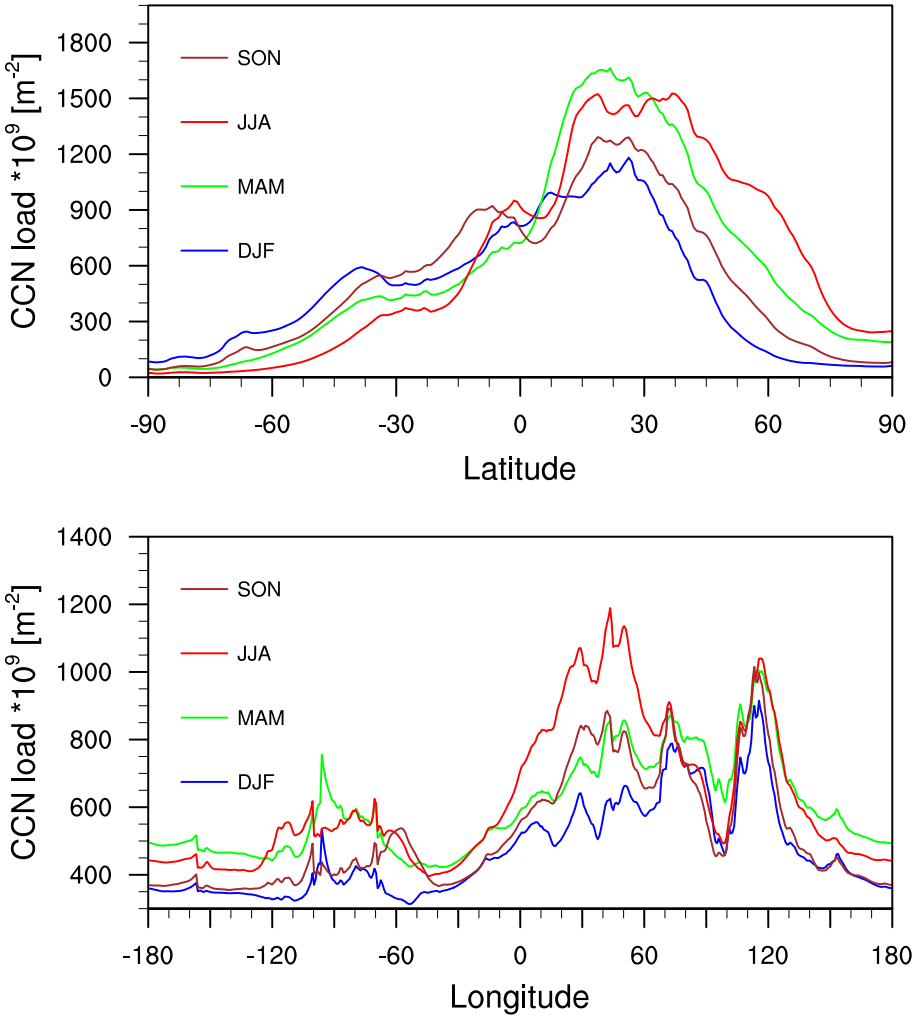

Figure 2. CCN load [$\times 10^9$ m^{-2}] of the lowermost 10 km at s = 0.2 %, averaged over longitudes (top) and over latitudes (bottom). CCN are averaged over seasons (SON, JJA, MAM, DJF) for the years 2003-2021, with Mauna Loa and Mexico City being excluded.

to decrease, while they are increasing in absolute terms for negative anomalies as can be seen especially for the last decade in Figure 3. The values of this decrease differ for the various supersaturations but the tendencies are robust. This behavior is not surprising as anthropogenic aerosol emissions have declined in most parts of the world following air quality policies (Szopa et al., 2021). Emissions of anthropogenic primary aerosol (mostly SU) and aerosol precursors (mostly SO_2) have decreased in the last 20 years, and these trends are reflected in observations of aerosol abundance (Quaas et al., 2022). SU emissions were mostly declining since 2000, with substantial declines over North America and Europe in particular. Declining trends can also be found over remote oceanic regions, where ship emissions have declined since 2010 following emission control protocols. Over China, the anthropogenic aerosol emissions have been increasing until around 2010, and decreasing thereafter. Over

https://doi.org/10.5194/essd-2023-172
Preprint. Discussion started: 17 July 2023

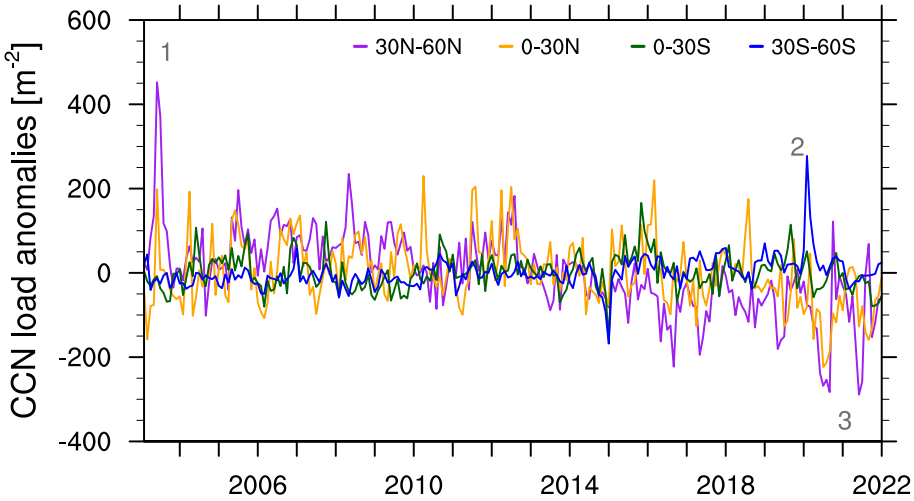

Figure 3. Anomalies of CCN load [$\times 10^9$ m^{-2}] over the entire atmospheric depth at 0.2 % supersaturation, averaged over 4 latitudional bands between 60° S and 60° N. The monthly mean anomaly is computed by subtracting the multi-year monthly mean over the entire timeseries from 2003 to 2021, with Mauna Loa and Mexico City being excluded. Numbers in grey illustrate specific showcase events.

Southeast Asia, including India, and also over parts of Africa, anthropogenic emissions showed increasing trends throughout the period 2000–2019. OC and BC emissions also show increasing trends which are more widespread, especially over more regions in East Asia, Africa, and also South America. These trends are mostly reflected in CAMS and therefore appear in CCN abundance.

3.2 CCN species contributions derived from CAMS

Figure 4 shows the global distributions of the four aerosol species contributing to total CCN for $s = 0.2\,\%$ which is presented in previous Figures. The plotted CCN are concentrations [cm^{-3}] near the surface, taken from the lowest model level. Therefore, in contrast to CCN load, emissions play a larger role than advection or aerosol physical processes. The SU CCN pattern shows a clear inter-hemispheric gradient, presenting most of the industrial and therefore SU emissions over the NH continents, with the largest emissions over China. Total CCN concentrations closely follow the distribution of sulfate since it has by far the highest concentration.

OM and BC CCN patterns are similar as both species are linked to the combustion of fossil fuel, biofuel and biomass. OM emissions additionally originate from terrestrial and marine biogenic ecosystems. They both show high concentrations over China, northern India, and the tropical rain forests. OM has larger amounts of CCN and is more spread out than BC which, apart from additional sources, might be due to the different hydrophilic fractions at emission. Even if we would assume absolute equal and constant emission rates of BC and OM, there is still 84 % hydrophilic OM but only 20 % hydrophilic BC which can act as CCN. The largest amount of SS CCN can be found over the Southern Ocean and along the storm tracks in the North

https://doi.org/10.5194/essd-2023-172
Preprint. Discussion started: 17 July 2023

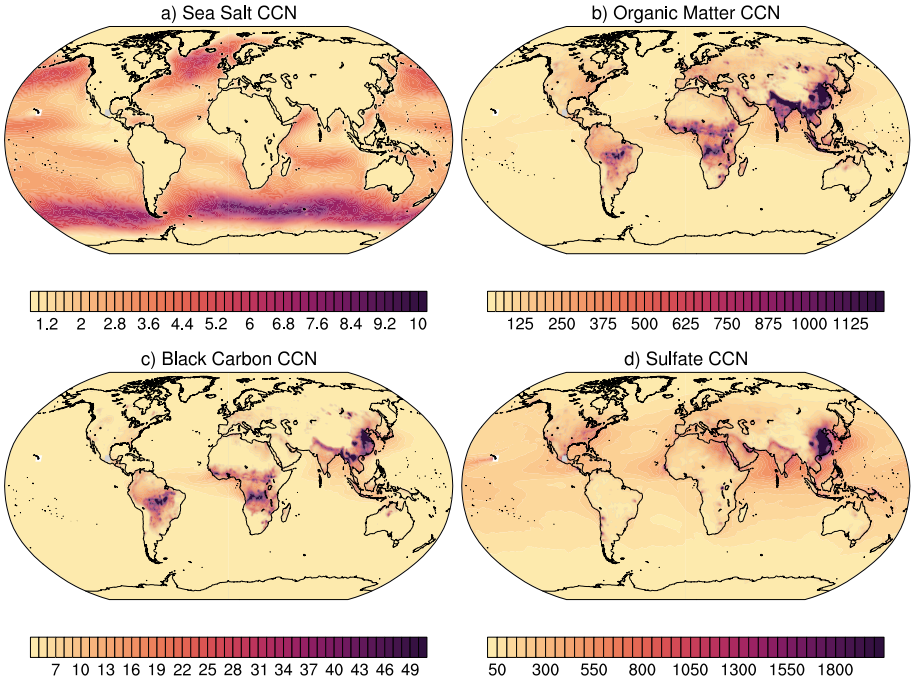

Figure 4. Near-surface CCN concentrations [cm^{-3}] at 0.2 % supersaturation of the 4 contributing species a) sea salt (sum of 3 size groups), b) hydrophilic organic matter, c) hydrophilic black carbon and d) sulfate. CCN are averaged in time for the year 2007, with Mauna Loa and Mexico City being excluded. Please note the different scales on the color bars.

Atlantic. SS CCN are noticeable in large storms, when surface wind speed are high and vertical mixing is enhanced.

Figure 5 shows the contribution of the four aerosol species to the total amount of CCN at 0.2 % supersaturation. The total CCN amount is mostly divided by contributions from SU and OM. SU dominates worldwide, except for the tropical rainforest areas and parts of Asia where OM is prevalent. At high latitudes SU and OM contributions often balance each other. Contributions from SS are negligible except over the Southern Ocean between 30° and 60° S. Even though SS is highly soluble and has the largest κ value, it is a big aerosol, associated with a large aerosol mass but low aerosol numbers. BC has low contributions even in regions of heavy biomass burning. This is due to the consideration of only 20 % as hydrophilic, and due to the smallest BC particle size, which requires larger supersaturations to activate in comparison to the other aerosol components.

Figure 6 shows the variability of each CCN species over the year. For a better comparison, we have normalized the near-surface monthly mean concentrations taken from the entire time period 2003 - 2021 by dividing them by their respective time mean. This means, values of CCN variability cannot be compared between species. In the global mean, SU CCN show almost no variation over the year because NH and SH variabilities cancel each other. In each hemisphere, SU CCN are higher in the respective hemisphere's summer than in the wintertime. Because SU is a dominant contributor to total CCN, this means that total CCN loads shift between hemispheres over the year with higher concentrations in the NH during boreal summer (JJA)

https://doi.org/10.5194/essd-2023-172
Preprint. Discussion started: 17 July 2023

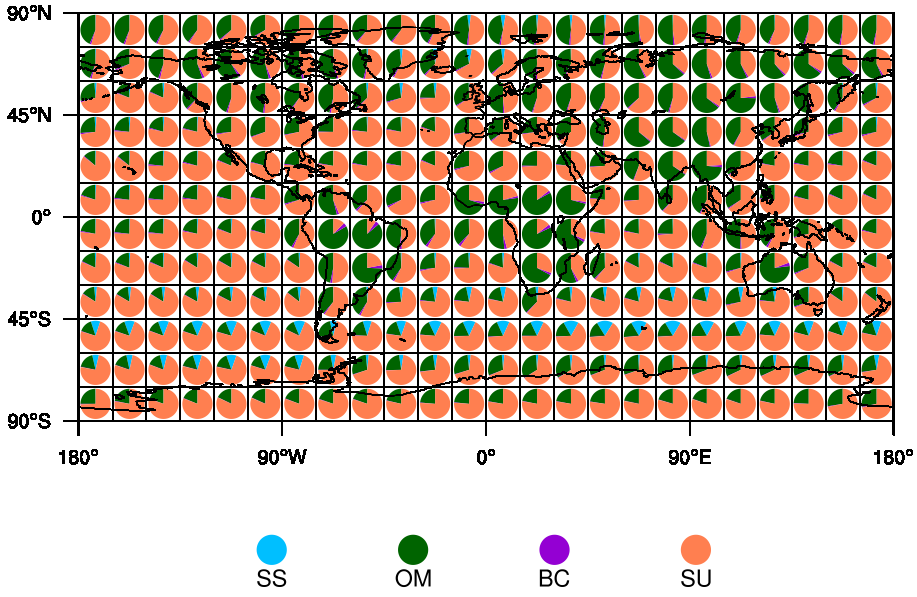

Figure 5. Contribution percentages of the four CCN aerosol species sea salt (SS, sum of 3 size groups), hydrophilic organic matter (OM), hydrophilic black carbon (BC) and sulfate (SU) at s = 0.2 % averaged for the year 2007, with Mauna Loa and Mexico City being excluded. Each pie-chart is produced of a $15^\circ \times 15^\circ$ average from near-surface data. Please note that the pie-charts do not reflect total CCN amount.

and higher concentrations in the SH during austral summer (DJF). Global mean OM and BC CCN seem to peak twice during the year, however the peak in spring originates from larger emissions in the NH while the peak in autumn originates from increased emissions in the SH. SS concentrations are highest in the wintertime months over the NH and in the summer months over the SH, which is due to enhanced wind speeds in these months. In the global mean, these variations cancel each other. Overall, each CCN species varies most naturally over the year and no larger anthropogenic impact on these variations can be found.

3.3 CCN validation

CAMS derived CCN are briefly evaluated here with quality assured data from the Atmospheric Radiation Measurement (ARM) network which were available within the time frame of CAMS (and MACC, for comparison see Block (2018)) and originate from the same instrument for better comparison. The ARM surface sites used here are located in very different aerosol environments ranging from remote to highly polluted. Users are encouraged to extent this first validation with observations or retrievals of their choice. CCN concentrations are measured at several supersaturations using a Droplet Measurement Technologies (DMT) single-column CCN counter (Roberts and Nenes, 2005). The instrument steps through several supersaturations in a pyramid like profile with 7 intervals (0.1, 0.2, 0.4, 0.6, 0.9, 1.1 and 1.2 %) in a cycle of 30 min with 5 min at each setting. The different supersaturations are obtained by variation of the chamber wall temperature and are calibrated using salt aerosol (static calibration). Additionally, supersaturations are also calculated using a heat transfer and fluid dynamics flow model (Lance et al.,

https://doi.org/10.5194/essd-2023-172
Preprint. Discussion started: 17 July 2023

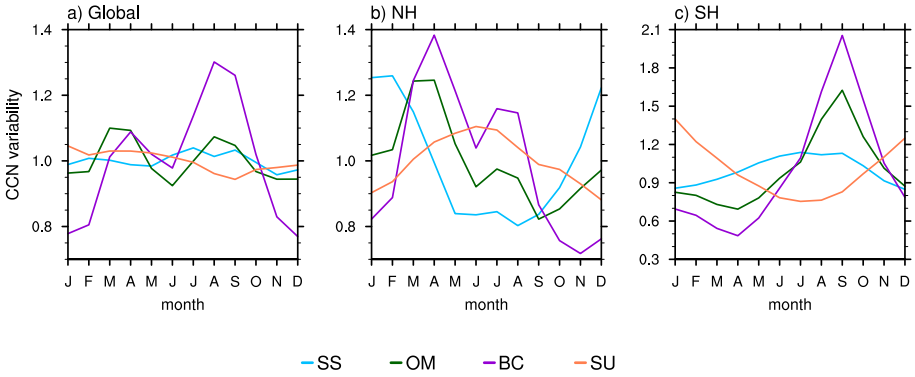

Figure 6. Relative variability of near-surface CCN species at 0.2 % supersaturation. Multi-year (2003-2021) monthly means of CCN concentrations are divided by the time mean to produce a normalized variability for each of the 4 contributing species: sea salt (SS, sum of 3 size groups), hydrophilic organic matter (OM), hydrophilic black carbon (BC) and sulfate (SU). Shown are averages over a) the entire globe, b) the northern hemisphere and c) the southern hemisphere, all with Mauna Loa and Mexico City being excluded.

2006) which are more reliable than the static calibrated ones (Shi et al., 2013). The instrument calibration and uncertainties involved are discussed in Rose et al. (2008). Spracklen et al. (2011) analyzed extensive CCN observations and found a range of uncertainties from 5-40 % depending on CCN concentration, supersaturation and the type of CCN instrument used. Their findings suggest a relative uncertainty of $\pm 40\,\%$ and a minimum absolute uncertainty of $\pm 20\,\mathrm{cm}^{-3}$, which is assumed here as well.

We have chosen to use the Aerosol Observing System Cloud Condensation Nuclei Average (AOSCCNAVG) value-added product (VAP) (Shi et al., 2013) because it consolidates the relevant CCN parameters into a single file and averages the data over the 5-minute integration time for each s value. Since the first minute of each s setting is unstable in terms of temperatures and the s value overshoots the setpoint, only the last four minutes are taken into account.

Table 2. Atmospheric Radiation Measurement (ARM) network sites and measurement periods used for CCN evaluation.

Site ID	Site/Campaign	Environment	Dataset	Time period (month/year)
SGP	Southern Great Plains: Central Facility, Lamont, OK, USA	rural	C1	01/2011-12/2012
PVC	Cape Cod: Highland Center, Cape Cod, MA, USA	coastal	M1	07-12/2012
PGH	Ganges Valley: ARIES Observatory, Nainital, Uttarkhand, India	mountainious	M1	06/2011-03/2012
GRW	Graciosa Island: Azores, Portugal	marine	M1	04/2009-12/2010
MAG	MAGIC: Los Angeles, CA to Honolulu, HI, USA - container ship Horizon Spirit	marine	M1	10-12/2012

https://doi.org/10.5194/essd-2023-172
Preprint. Discussion started: 17 July 2023

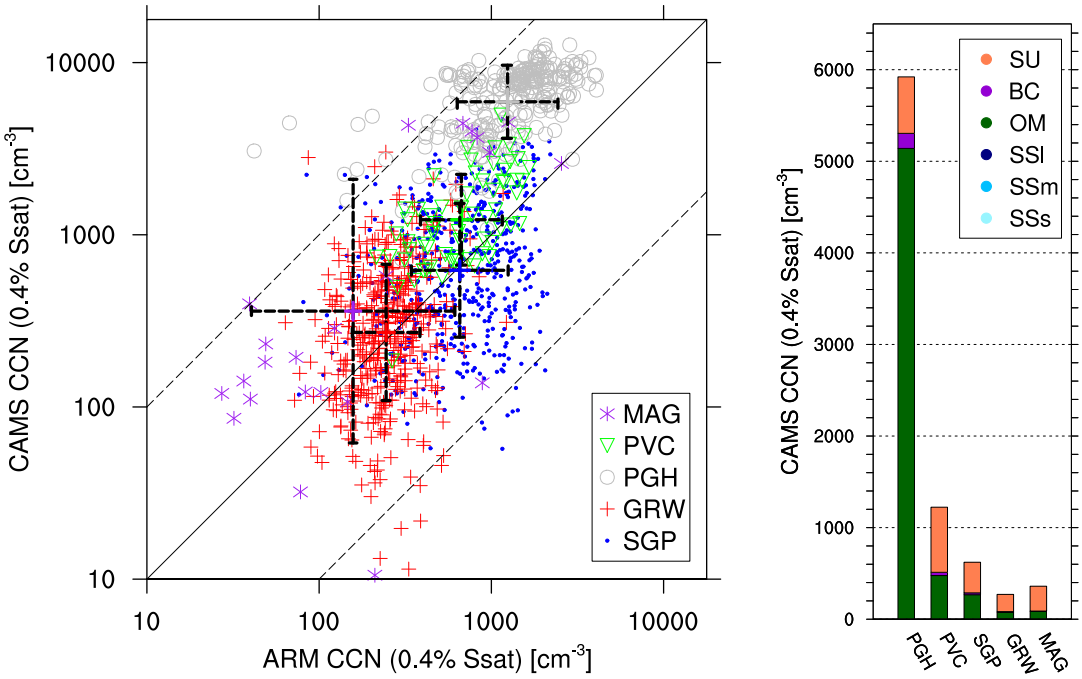

(a) CAMS vs. ARM CCN data near the surface. Average (colored cross) and standard deviations (vertical and horizontal bar) are computed from logarithmic values for each station.

(b) CAMS CCN species contributions at ARM sites, corresponding to panel (a).

Figure 7. Validation of CAMS CCN concentration with ARM surface site data for 0.4 % supersaturation. The ARM stations are listed in Table 2.

The AOSCCNAVG VAP produces two output data streams, from which we have chosen to use the c2 output produced from the mentor-edited b1 level input datastreams. The data are taken from four land stations. Additionally we have taken AOS CCN data (not VAP) from the Marine ARM GPCI Investigation of Clouds (MAGIC) project which is a ship campaign in the Pacific. The sites, datasets and measurement times used, are listed in Table 2.

We use daily means of quality-checked CCN measurements and ensured that each day comprises statistically stable values which can be compared to CAMS derived CCN once a day. The comparison to CAMS CCN is done for a single supersaturation at 0.4 % for reasons of convenience. For detailed description of data handling, please see Appendix B.

The evaluation of the CAMS reanalysis $CCN_{0.4}$ with ARM data (Fig. 7, (a)) reveals a good agreement considering the large range of magnitudes. A share of 96.5 % of the data lies within a factor of 10. As expected, the lowest CCN concentrations are found for clean marine conditions (GRW and MAG), which are followed by conditions with medium aerosol concentrations (SGP and PVC). The spread of data points is largest for MAG site (see NRMSE in Table 3) which might be due to the low amount of observed data. The Indian site (PGH), which is found to be in one of the most polluted regions in the world, shows by far the highest model CCN concentrations. The CCN species contributions of the individual stations, also presented in Fig. 7,

https://doi.org/10.5194/essd-2023-172
Preprint. Discussion started: 17 July 2023

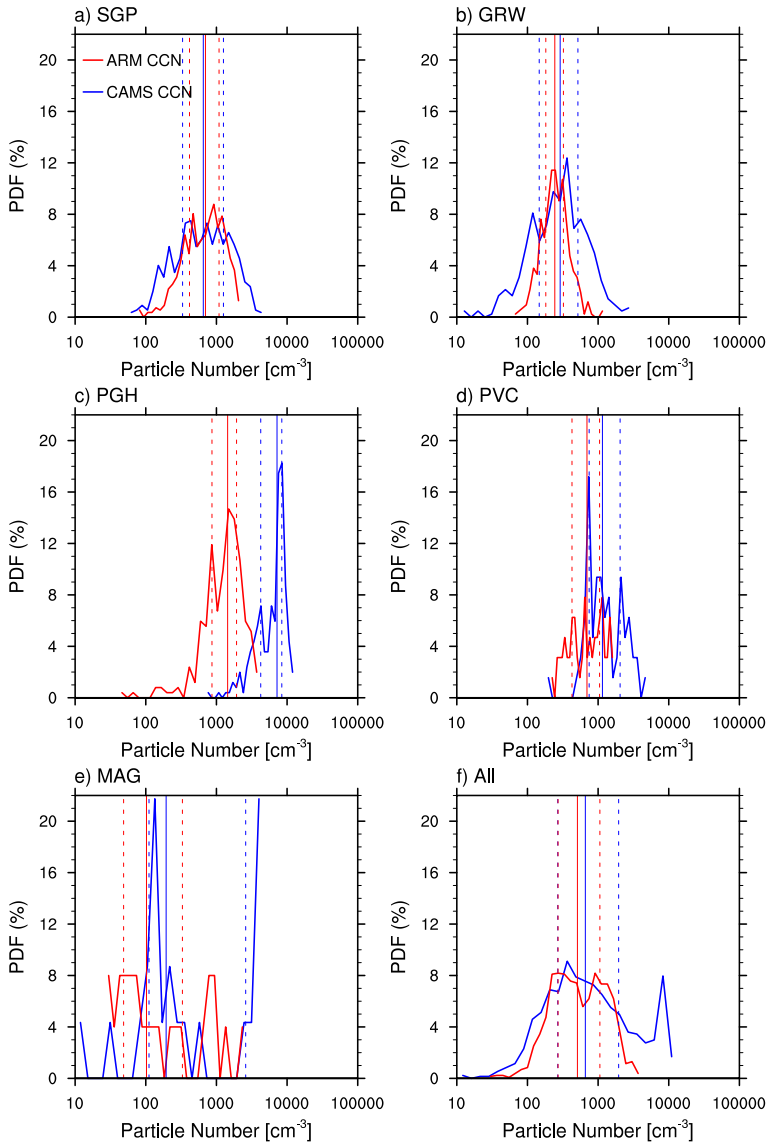

Figure 8. CAMS vs. ARM CCN probability density functions, for CCN taken at 0.4 % S_{sat} near the surface. The PDFs are shown for the the ARM sites listed in Table 2, with all stations taken together in Panel f). CAMS data are plotted in blue and ARM data in red. The vertical lines indicate the medians (solid lines) and the interquartile range (dashed), with one line at the 25th, and the other at the 75th percentile, of each distribution.

(b), reveals almost balanced contributions from sulfate and organic matter for all stations, except for PGH where OM is by far the most dominant species. In comparison, sea salt concentrations are negligible, even for marine sites.

As can be seen from Figure 8, the simulated total CCN mostly overestimate the observations (except for SGP) in terms of median and interquartile range (except for PGH). The results are summarized in Table 3. However, taking into account

https://doi.org/10.5194/essd-2023-172
Preprint. Discussion started: 17 July 2023

Table 3. CCN evaluation with ARM data, given the measurement uncertainties σ_{m} in %. The probability distribution characteristics as shown in Fig. 8 are given by the median Q_{50}, the 25th percentile Q_{25} and the 75th percentile Q_{75} of the CCN concentrations in [cm^{-3}]. The bias(Q_{50}) is a factor computed by dividing the CAMS CCN Q_{50} by the ARM Q_{50}, regarding measurement uncertainties in square brackets, while bias(IQR) is the bias of the interquartile range computed in the same manner. The last column indicates the normalized root mean square error (NRMSE) in %. It is calculated from the root mean squared error of logarithmic values, divided by $\log(Q_{50})$ of the observations.

Site ID	days	data	σ_m [%]	Q_{25} [cm^{-3}]	Q_{50} [cm^{-3}]	Q_{75} [cm^{-3}]	bias(Q_{50})	bias(IQR)	NRMSE [%]
MAG	23	ARM CAMS	40.0	48 ± 19 111	102 ± 41 194	330 ± 132 2595	1.9 [1.36,3.16]	3.44 [1.47,8.02]	31.7
GRW	420	ARM CAMS	40.0	182 ± 73 147	244 ± 98 290	323 ± 129 518	1.19 [0.85,1.99]	1.99 [0.85,4.64]	16.8
PVC	64	ARM CAMS	40.0	427 ± 171 747	696 ± 278 1151	1049 ± 420 2048	1.66 [1.18,2.76]	1.12 [0.48,2.60]	11.8
SGP	547	ARM CAMS	40.0	416 ± 166 332	699 ± 280 652	1089 ± 436 1257	0.93 [0.67,1.55]	1.45 [0.62,3.37]	14.9
PGH	252	ARM CAMS	40.0	865 ± 346 4237	1440 ± 576 7205	1927 ± 771 8421	5.0 [3.57,8.34]	0.89 [0.38,2.08]	22.8
All	1306	ARM CAMS	40.0	270 ± 108 268	509 ± 204 659	1059 ± 424 1954	1.29 [0.92,2.16]	1.86 [0.8,4.34]	18.1

the measurement uncertainties (values given in square brackets) the CCN retrieved from the CAMS reanalysis are reasonable within the range of the measurements. Only the bias for PGH is out of bounds, introducing a spike in the CCN distribution which is outside the range of observations (Figure 8, f). As stated in Inness et al. (2019b), some improvements of CAMSRA in comparison to the previous version MACC (Inness et al., 2013; Mangold et al., 2011; Benedetti et al., 2009; Morcrette et al., 2009) are accompanied by a large increase in organic matter in polluted regions from the introduction of a representation of anthropogenic SOA. It could be argued here, that this is the cause for the large deviation found at the PGH site. It is unclear to what extent this erroneous overestimation of CCN concerns other heavily polluted areas and it needs further validation to find the source of this feature. Because of this, the overall bias of the log-normal distributions of all the stations taken together is + 29 %, with an overestimation in variability by 86 %. Note, that even if PGH showed a perfect fit (CCN divided by 5), still the overall bias overestimation would be $+21\,\%$ with an overestimation in variability of 23 %. This shows, that the overestimation at PGH mainly concerns the width of the CCN number distribution.

The correlation coefficients (Table 4) clearly show the improvement of CAMS CCN over AOD as a proxy for CCN (Andreae, 2009), when compared to near-surface CCN measurements. The overall correlation coefficient increases by a factor of 1.9 when

https://doi.org/10.5194/essd-2023-172
Preprint. Discussion started: 17 July 2023

using CAMS CCN instead of AOD as a proxy for observed CCN. The strongest improvements are found for the GRW station. A study of Logan et al. (2014) shows that the Azores (GRW site) experiences a range of aerosol conditions with mixtures of dust, pollution and smoke. They found rather weak correlations between aerosol loading and CCN due to mineral dust influences, while events with sulfate content within volcanic ash and pollution particles showed strong relationship with CCN. Regarding their findings, one reason for the improvement of R might be related to the fact that DU is neglected here as potential CCN due to its insoluble character, even though this is debatable regarding the findings of Karydis et al. (2011) who argue that even freshly emitted dust lacking any soluble material can still act as a good CCN. Another advantage of CAMS derived CCN is the vertical resolution that enables filtering aerosol layers. e.g. from long-range transport. These layers can increase column AOD without actually increasing CCN at the relevant height (in this case near the surface), leading to lower correlations. However, the highest correlations are found for the remote marine site (MAG), where MODIS AOD is supposed to work best (Remer et al., 2005). Still, even for this site the correlation to observations by CAMS CCN is slightly enhanced in comparison to AOD. Since the assimilation of AOD is limited to the regions between 70° S and 70° N, CAMS retrieved CCN might deviate more from observations in the polar regions since they are not constrained and we suggest to only use CCN data outside of the polar circles.

The general correlation of $R = 0.71$ shows that the reanalysis CCN fits well to the surface observations. The results show that the correlation coefficient to measured CCN almost doubles when using CCN from the reanalysis instead of AOD. This results from the resolved vertical distribution and the aerosol speciation in the CAMS reanalysis.

Table 4. CCN-AOD correlation coefficients. CCN corresponds to CCN($s = 0.4\,\%$), either observed ($\mathrm{CCN_{ARM}}$) or from the reanalysis ($\mathrm{CCN_{CAMS}}$). $\mathrm{AOD_{MODIS}}$ is the "Dark_Target_Deep_Blue_Optical_Depth_550_Combined" as described in Levy et al. (2013), retrieved from MODIS (collection 6 on board of Aqua), available daily on a 1 x 1° grid (MYD08_D3 data product), used in here from 2003 - 2014. The Pearson correlation coefficients R are computed using the logarithm of data values for which all three datasets were available - in total 748 points. The last row presents the results if all the stations were taken together as in Fig. 8, f.

Site ID	R ($\mathrm{CCN_{CAMS}}$ vs. $\mathrm{CCN_{ARM}}$)	R ($\mathrm{AOD_{MODIS}}$ vs. $\mathrm{CCN_{ARM}}$)
MAG	0.76	0.65
GRW	0.18	0.07
PVC	0.66	0.44
SGP	0.24	0.25
PGH	0.41	0.28
All	0.71	0.37

4 Conclusions

The CAMS reanalysis has been used to produce a 19 year long 3-D CCN climatology, which has been analyzed and evaluated here. Since the reanalysis links modeled aerosols with observed AOD, the resulting total CCN are constrained by AOD

https://doi.org/10.5194/essd-2023-172
Preprint. Discussion started: 17 July 2023

observations from satellites. Therefore this climatology offers a unique opportunity to be used for studies of aerosol-cloud interactions in an observationally constrained global framework.

There are several advantages of using this reanalysis CCN rather than using AOD as a CCN proxy, as was commonly done in previous observational studies of aerosol-cloud interactions. First, the reanalysis CCN have a global, spatio-temporally continuous coverage while AOD can only be retrieved for cloud free regions at satellite overpass time. Second, the reanalysis CCN are vertically resolved while AOD is a column integrated quantity. This provides the opportunity to retrieve CCN at cloud base heights, where activation occurs. Third, the reanalysis provides mass concentrations of four CCN relevant aerosol species which are black carbon, organic matter, sulfate and sea salt. Therefore the chemical and size determined potential of each aerosol species to act as CCN is taken into account, which is not possible from AOD to that accuracy. Furthermore, hygroscopic growth of the aerosols is taken into account in the IFS when computing optical properties. This reduces uncertainties associated with hygroscopic effects enhancing AOD without actually increasing CCN numbers.

The CCN climatology is available daily from 2003 to 2021, on a Gaussian grid at a resolution of 80 km and 60 vertical levels. It is derived from the CAMS reanalysis on the corresponding grid (TL255L60), using the models given parameters of aerosol lognormal size distribution and by applying a modified κ-Köhler framework. For deriving number concentrations from the given CAMS mass mixing ratios, the same aerosol size distribution for external mixtures was applied that was initially used in the IFS aerosol scheme for obtaining aerosol optical properties and converting between aerosol mass and assimilated AOD. This ensures that the proportionality between CCN and AOD is kept and any improvements of derived reanalysis CCN over observed AOD can therefore only result from the vertical distribution and the modeled CCN relevant aerosol specifications and processes.

The resulting CCN distribution shows very clearly the dependence on modeled aerosol processes, such as emission, advection and scavenging. Concentrations are pronounced in the NH mid-latitudes where anthropogenic emissions dominate. Globally, CCN are dominated by sulfate aerosol and organic matter. Black carbon only occurs more dominantly in connection with wildfires and biomass burning events. Contributions from sea salt are negligible except over the Southern Ocean. Total CCN and CCN species show realistic distributions and variabilities.

A brief validation with in-situ surface observations has shown, that total CCN are modeled well in the range of CCN measurements. However, we found a bias factor of 1.29, compared to the surface in-situ observations used here and an overall overestimation of the CCN spectrum. This is partly because of too high OM contributions in an already very polluted site. We suggest more validation in order to find the source of overestimation. This also indicates that the aerosol specification is less reliable than the total CCN amount, since the species fraction to total aerosol mass is not influenced by the assimilated AOD.

However, even with this rather simplistic 1-moment aerosol scheme, the results show that the simulated total CCN agree well with surface observations, with R = 0.71. In comparison to AOD with R = 0.37, the correlation coefficient almost doubles. This result shows that refining the observed column AOD by a vertical distribution and an aerosol speciation, including effects of hygroscopicity, clearly improves estimations of CCN. The final outcome is mainly a matter of how realistic the aerosol processing in a certain model is. In this case, the CCN climatology derived here from the CAMS reanalysis provides a new

https://doi.org/10.5194/essd-2023-172
Preprint. Discussion started: 17 July 2023

benchmark for improving assessments of aerosol-cloud interactions in particular because of its global coverage and its possible usage in Earth System Models.

5 Data availability

The data is freely accessible at https://doi.org/10.26050/WDCC/QUAERERE_CCNCAMS_v1 from the World Data Centre for Climate (WDCC) for registered users. When using the data, please cite as: Block, Karoline (2023). Cloud condensation nuclei (CCN) numbers derived from CAMS reanalysis EAC4 (Version 1). World Data Center for Climate (WDCC) at DKRZ. https://doi.org/10.26050/WDCC/QUAERERE_CCNCAMS_v1.

Appendix A: The modified Köhler theory

The theory of heterogeneous droplet nucleation is founded on the work of Hilding Köhler (Köhler, 1936) who determined the equilibrium radius of particles as a function of dry radius r_d and relative humidity RH (Seinfeld and Pandis, 2006). We refer to the formulation of this relationship as the Köhler equation written as (Seinfeld and Pandis, 2006; Pruppacher and Klett, 1997)

$$\ln S = \frac{4M_w\sigma_{w/a}}{RT\rho_w D_w} - \frac{\phi_s \varepsilon \nu \rho_d M_w D_d^3}{\rho_w M_d D_w^3} = \frac{A}{D_w} - \frac{B}{D_w^3} \tag{A1}$$

$$\text{with} \quad A = \frac{4M_w\sigma_{w/a}}{RT\rho_w} \quad \text{and} \quad B = \frac{\phi_s \varepsilon \nu \rho_d M_w}{\rho_w M_d} D_d^3 = K D_d^3 \,.$$

Equation A1 gives saturation ratio S at a specific temperature at which a droplet is in equilibrium with its environment as a function of the wet droplet diameter D_w, the dry aerosol particle diameter D_d and the hygroscopicity of the aerosol particle. The curvature parameter A contains the surface tension parameter $\sigma_{w/a}$, the universal gas constant R, temperature T, the molar mass of water M_w and the water density ρ_w. It shows that at any given temperature the equilibrium vapor pressure over a curved interface exceeds that of the same substance over a flat surface, and even more so the smaller the droplet is (Seinfeld and Pandis, 2006).

The hygroscopicity parameter B contains the mass fraction of soluble material ε, the osmotic coefficient ϕ_s, the number of ions ν that a molecule dissociated into when dissolved in water, the dry aerosol density ρ_d and aerosol molar mass M_d, the molar mass of water M_w and the water density ρ_w as well as the dry aerosol particle diameter D_d.

As we can see from the B parameter, it cannot be easily obtained and is very complex. In order to characterize the relative hygroscopicities of individual aerosol constituents, known mixtures, and complex atmospheric aerosols, Petters and Kreidenweis (2007) introduced a hygroscopicity parameter κ which simplifies the hygroscopicity parameter B and obviates the need to determine, or assume, aerosol properties such as dry particle density, molecular weight, and dissociation constants (Petters and Kreidenweis, 2007).

https://doi.org/10.5194/essd-2023-172
Preprint. Discussion started: 17 July 2023

$$S = \alpha_w \cdot \exp\left(\frac{4M_w\sigma_{w/a}}{RT\rho_w D_w}\right) \quad \text{with} \quad \frac{1}{\alpha_w} = 1 + \kappa\frac{V_d}{V_w} \tag{A2}$$

with κ being defined through its effect on the water activity of the solution α_w, V_d being the volume of the dry particulate matter and V_w being the volume of the water. With some further reconstructions (see Petters and Kreidenweis (2007)), this evolves into Eq. 3, stated here again as

$$S(D_w) = \frac{D_w^3 - {D_d}^3}{D_w^3 - {D_d}^3(1-\kappa)} \cdot \exp\left(\frac{4\sigma_{w/a}M_w}{RT\rho_w D_w}\right) \text{with} \quad \alpha_w = \frac{D_w^3 - {D_d}^3}{D_w^3 - {D_d}^3(1-\kappa)}\,. \tag{A3}$$

Now, we modify this equation as in Pöhlker et al. (2023). Assuming supersaturations $s \ll 1$, we can approximate $\ln S = \ln(1+s) \approx s$, and with assuming $D_d \ll D_w$, it becomes

$$\ln S \approx s = \ln\left(\frac{D_w^3 - {D_d}^3}{D_w^3 - {D_d}^3(1-\kappa)}\right) + \left(\frac{4M_w\sigma_{w/a}}{RT\rho_w D_w}\right) = \ln\left(\frac{D_w^3 - {D_d}^3}{D_w^3 - {D_d}^3(1-\kappa)}\right) + \frac{A}{D_w} \tag{A4}$$

$$\begin{aligned} s &= \frac{A}{D_w} - \ln\left(\frac{D_w^3 - (1-\kappa){D_d}^3}{D_w^3 - {D_d}^3}\right) \\ &= \frac{A}{D_w} - \ln\left(1 + \frac{\kappa D_d^3}{D_w^3 - D_d^3}\right) \\ &\approx \frac{A}{D_w} - \frac{\kappa D_d^3}{D_w^3 - D_d^3} \\ &\approx \frac{A}{D_w} - \kappa\frac{D_d^3}{D_w^3} \end{aligned} \tag{A5}$$

As we can see, even for our set conditions of low supersaturations, this relation holds according to the traditional Köhler formulation, but with $K = \kappa$.

Appendix B: ARM data treatment

CCN evaluation with ARM data was done for daily means of quality checked data. Wood et al. (2017) found that for the GRW data, there was an abnormal degradation in CCN concentrations from October 2009 to June 2010. The values returned back to normal (in comparison to concentrations from the CN counter) after the instrument was maintained thoroughly. They corrected the data using monthly multiplication factors to obtain a stable ratio between CCN and NC, assuming that the CN counter was correct. In this study we also use the corrected dataset from Wood et al. (2017).

Special care is taken for the daily mean statistics, which is used to compute CCN at 0.4 % s. To ensure a statistically stable result, only CCN data retrieved at at least 4 of the 7 s-bins with a minimum of total 96 measurements per day (1/3 of maximum possible data coverage) are taken into account. Further we neglect data which seem to have artefacts like a systematic significant

https://doi.org/10.5194/essd-2023-172
Preprint. Discussion started: 17 July 2023

increase of NC with supersaturation. This was mainly found for GRW data. Therefore, the corrected dataset from Wood et al. (2017) was only applied on days with good daily statistics.

The comparison to CAMS CCN is done for a single supersaturation at 0.4 % for reasons of convenience. Were there enough data at 0.4 % s available, the daily average was simply taken from those measurements. Otherwise, the measured data from the various s-bins were converted to $CCN_{0.4}$ as is done in Andreae (2009), using Twomey's power law (Twomey, 1959; Seinfeld and Pandis, 2006)

$$CCN(s) = CCN(s = 1\%) \cdot s^k. \tag{B1}$$

Solving Equation B1 for k,

$$k = \frac{1}{\ln s} \cdot \ln\left(\frac{CCN_{0.4}}{CCN_{1.0}}\right), \tag{B2}$$

and transforming it to a more general form, regarding that $\ln(s = 1\%) = 0$,

$$\ln CCN_2 - \ln CCN_1 = k \cdot (\ln s_2 - \ln s_1), \tag{B3}$$

one obtains this simple form

$$\ln CCN_{0.4} = k \cdot \ln\left(\frac{0.4}{s}\right) + \ln CCN(s). \tag{B4}$$

Taking the exponential of Equation B4, we obtain the final form, which is used in this study to convert CCN at any measured s to 0.4 %

$$CCN_{0.4} = CCN(s) \cdot \left(\frac{0.4}{s}\right)^k. \tag{B5}$$

The exponent k is computed from linear regression between logarithmic s and the respective CCN. The actual behaviour of CCN with s is not exactly following the power law. A demonstration and a possible extension of the formular is given in Cohard et al. (1998). This deviation has been accounted for by the standard deviation of k. But since this only adds about 1-3 % uncertainty to $CCN_{0.4}$, it can be neglected compared to the 40 % measurement uncertainty.

Author contributions. Data analysis, including coding the box model, running the code on CAMS data, validation and ARM data handling, creating statistical analyses, plots, tables and text by main author Karoline Block. Help in setting up the initial box model version by Daniel Partridge. Downloading and handling CAMS data, helping with the analysis and bug fixes in the box model by Mahnoosh Haghighatnasab. Project advise, valuable input and proof read by Philip Stier. Project lead, corrections and proof read by Johannes Quaas.

Competing interests. The authors declare that they have no conflict of interest.

https://doi.org/10.5194/essd-2023-172
Preprint. Discussion started: 17 July 2023

Acknowledgements. Thus study was supported by the European Union through the Horizon2020 project MACC-III (grant agreement 633080), the COPERNICUS Atmospheric Monitoring Service (CAMS-74, radiative forcing), European Research Council (ERC) Starting Grant QUAERERE (GA 306284), and Horizon 2020 project CONSTRAIN (GA 820829).

The CCN dataset produced for this study is generated using Copernicus Atmosphere Monitoring Service information (2003 - 2021). Neither the European Commission nor ECMWF is responsible for any use that may be made of the Copernicus information or data it contains. The CAMS data were downloaded from the Copernicus Atmosphere Monitoring Service (CAMS) Atmosphere Data Store (ADS) (https://ads.atmosphere.copernicus.eu/cdsapp#!/dataset/cams-global-reanalysis-eac4?tab=overview).

ARM data were obtained from the Atmospheric Radiation Measurement (ARM) user facility (https://www.arm.gov/data/), a U.S. Department Of Energy (DOE) office of science user facility managed by the Biological and Environmental Research Program. Data correction for the GRW site was kindly provided by Robert Wood.

The MODIS products used in this study are from the NASA Goddard Space Flight Center and available from the Atmosphere Archive and Distribution System (http://ladsweb.nascom.nasa.gov).

https://doi.org/10.5194/essd-2023-172
Preprint. Discussion started: 17 July 2023

References

Abdul-Razzak, H., Ghan, S. J., and Rivera-Carpio, C.: A parameterization of aerosol activation: 1. Single aerosol type, J. Geophys. Res., 103, 6123–6131, https://doi.org/10.1029/97JD03735, 1998.

Ackerman, T. P. and Toon, O. B.: Absorption of visible radiation in atmosphere containing mixtures of absorbing and non-absorbing particles, Appl. Opt., 20, 3661–3667, https://doi.org/10.1364/AO.20.003661, 1981.

Andreae, M. O.: Correlation between cloud condensation nuclei concentration and aerosol optical thickness in remote and polluted regions, Atmos. Chem. Phys., 9, 543–556, https://doi.org/10.5194/acp-9-543-2009, 2009.

Asmi, A., Wiedensohler, A., Laj, P., Fjaeraa, A.-M., Sellegri, K., Birmili, W., Weingartner, E., Baltensperger, U., Zdimal, V., Zikova, N., Putaud, J.-P., Marinoni, A., Tunved, P., Hansson, H.-C., Fiebig, M., Kivekäs, N., Lihavainen, H., Asmi, E., Ulevicius, V., Aalto, P. P., Swietlicki, E., Kristensson, A., Mihalopoulos, N., Kalivitis, N., Kalapov, I., Kiss, G., de Leeuw, G., Henzing, B., Harrison, R. M., Beddows, D., O'Dowd, C., Jennings, S. G., Flentje, H., Weinhold, K., Meinhardt, F., Ries, L., and Kulmala, M.: Number size distributions and seasonality of submicron particles in Europe 2008-2009, Atmos. Chem. Phys., 11, 5505–5538, https://doi.org/10.5194/acp-11-5505-2011, 2011.

Bellouin, N., Quaas, J., Morcrette, J.-J., and Boucher, O.: Estimates of aerosol radiative forcing from the MACC re-analysis, Atmos. Chem. Phys., 13, 2045–2062, https://doi.org/10.5194/acp-13-2045-2013, 2013.

Bellouin, N., Quaas, J., Gryspeerdt, E., Kinne, S., Stier, P., Watson-Parris, D., Boucher, O., Carslaw, K., Christensen, M., Daniau, A.-L., Dufresne, J.-L., Feingold, G., Fiedler, S., Forster, P., Gettelman, A., Haywood, J. M., Lohmann, U., Malavelle, F., Mauritsen, T., McCoy, D., Myhre, G., Mülmenstädt, J., Neubauer, D., Possner, A., Rugenstein, M., Sato, Y., Schulz, M., Schwartz, S. E., Sourdeval, O., Storelvmo, T., Toll, V., Winker, D., and Stevens, B.: Bounding global aerosol radiative forcing of climate change, Rev. Geophys., 58, e2019RG000 660, https://doi.org/10.1029/2019RG000660, 2020.

Benedetti, A., Morcrette, J.-J., Boucher, O., Dethof, A., Engelen, R. J., Fisher, M., Flentje, H., Huneeus, N., Jones, L., Kaiser, J. W., Kinne, S., Mangold, A., Razinger, M., Simmons, A. J., and Suttie, M.: Aerosol analysis and forecast in the European Centre for Medium-Range Weather Forecasts Integrated Forecast System: 2. Data assimilation, J. Geophys. Res., 114, https://doi.org/10.1029/2008JD011115, D13205, 2009.

Block, K.: Aerosol-Cloud-Radiation Interactions in Regimes of Liquid Water Clouds, Ph.D. thesis, Universität Leipzig, https://nbn-resolving.org/urn:nbn:de:bsz:15-qucosa2-319314, 2018.

Block, K.: Cloud condensation nuclei (CCN) numbers derived from CAMS reanalysis EAC4 (Version 1), https://doi.org/10.26050/WDCC/QUAERERE_CCNCAMS_v1, 2023.

Boucher, O., Pham, M., and Venkataraman, C.: Simulation of the atmospheric sulfur cycle in the LMD GCM: Model description, model evaluation, and global and European budgets, Inst. Pierre-Simon Laplace, Paris, France., Note 23, 26 pp., http://icmc.ipsl.fr/images/publications/scientific_notes/note23.pdf, 2002.

Bozzo, A., Benedetti, A., Flemming, J., Kipling, Z., and Rémy, S.: An aerosol climatology for global models based on the tropospheric aerosol scheme in the Integrated Forecasting System of ECMWF, Geosci. Model Develop., 13, 1007–1034, https://doi.org/10.5194/gmd-13-1007-2020, 2020.

Choudhury, G. and Tesche, M.: Estimating cloud condensation nuclei concentrations from CALIPSO lidar measurements, Atmospheric Measurement Techniques, 15, 639–654, https://doi.org/10.5194/amt-15-639-2022, 2022.

Cohard, J., Pinty, J., and Bedos, C.: Extending Twomey's Analytical Estimate of Nucleated Cloud Droplet Concentrations from CCN Spectra, J. Atmos. Sci., pp. 3348–3357, https://doi.org/https://doi.org/10.1175/1520-0469(1998)055%3C3348:ETSAEO%3E2.0.CO;2, 1998.

Davies, T., Cullen, M. J. P., Malcolm, A. J., Mawson, M. H., Staniforth, A., White, A. A., and Wood, N.: A new dynamical core for the Met Office's global and regional modelling of the atmosphere, Quart. J. Royal Meteo. Soc., 131, 1759–1782, https://doi.org/10.1256/qj.04.101, 2005.

Flemming, J., Huijnen, V., Arteta, J., Bechtold, P., Beljaars, A., Blechschmidt, A.-M., Diamantakis, M., Engelen, R. J., Gaudel, A., Inness, A., Jones, L., Josse, B., Katragkou, E., Marecal, V., Peuch, V.-H., Richter, A., Schultz, M. G., Stein, O., and Tsikerdekis, A.: Tropospheric chemistry in the Integrated Forecasting System of ECMWF, Geoscientific Model Development, 8, 975–1003, https://doi.org/10.5194/gmd-8-975-2015, 2015.

Forster, P., Storelvmo, T., Armour, K., Collins, W., Dufresne, J.-L., Frame, D., Lunt, D., Mauritsen, T., Palmer, M., Watanabe, M., Wild, M., and Zhang, H.: The Earth's Energy Budget, Climate Feedbacks, and Climate Sensitivity, in: Climate Change 2021: The Physical Science Basis. Contribution of Working Group I to the Sixth Assessment Report of the Intergovernmental Panel on Climate Change, edited by Masson-Delmotte, V., Zhai, P., Pirani, A., Connors, S., Péan, C., Berger, S., Caud, N., Chen, Y., Goldfarb, L., Gomis, M., Huang, M., Leitzell, K., Lonnoy, E., Matthews, J., Maycock, T., Waterfield, T., Yelekçi, O., Yu, R., and Zhou, B., p. 923–1054, Cambridge University Press, Cambridge, United Kingdom and New York, NY, USA, https://doi.org/10.1017/9781009157896.009, 2021.

Ghan, S. J., Chuang, C. C., and Penner, J. E.: A parameterization of cloud droplet nucleation, I, single aerosol type, Atmos. Res., pp. 197–221, https://doi.org/10.1016/0169-8095(93)90024-I, 1993.

Grandey, B. S. and Stier, P.: A critical look at spatial scale choices in satellite-based aerosol indirect effect studies, Atmos. Chem. Phys., 10, 11 459–11 470, https://doi.org/10.5194/acp-10-11459-2010, 2010.

Granier, C., Bessagnet, B., Bond, T., D'Angiola, A., van der Gon, H., Frost, G., Heil, A., Kaiser, J., Kinne, S., Klimont, Z., Kloster, S., Lamarque, J., Liousse, C., Masui, T., Meleux, F., Mieville, A., Ohara, T., Raut, J., Riahi, K., Schultz, M., Smith, S., Thompson, A., van Aardenne, J., van der Werf, G., and van Vuuren, D.: Evolution of anthropogenic and biomass burning emissions of air pollutants at global and regional scales during the 1980–2010 period, Clim. Change, 109, https://doi.org/10.1007/s10584-011-0154-1, 2011.

Gryspeerdt, E. and Stier, P.: Regime-based analysis of aerosol-cloud interactions, Geophys. Res. Lett., 39, https://doi.org/10.1029/2012GL053221, L21802, 2012.

Gryspeerdt, E., Quaas, J., Ferrachat, S., Gettelman, A., Ghan, S., Lohmann, U., Morrison, H., Neubauer, D., Partridge, D. G., Stier, P., Takemura, T., Wang, H., Wang, M., and Zhang, K.: Constraining the instantaneous aerosol influence on cloud albedo, Proc. Nat. Acad. Sci. USA, 119, 4899–4904, https://doi.org/10.1073/pnas.1617765114, 2017.

Guenther, A., Karl, T., Harley, P., Wiedinmyer, C., Palmer, P. I., and Geron, C.: Estimates of global terrestrial isoprene emissions using MEGAN (Model of Emissions of Gases and Aerosols from Nature), Atmos. Chem. Phys., 6, 3181–3210, https://doi.org/10.5194/acp-6-3181-2006, 2006.

Haghighatnasab, M., Kretzschmar, J., Block, K., and Quaas, J.: Impact of Holuhraun volcano aerosols on clouds in cloud-system-resolving simulations, Atmospheric Chemistry and Physics, 22, 8457–8472, https://doi.org/10.5194/acp-22-8457-2022, 2022.

Hasekamp, O., Gryspeerdt, E., and Quaas, J.: Analysis of polarimetric satellite measurements suggests stronger cooling due to aerosol-cloud interactions, Nature Comm., 10, https://doi.org/10.1038/s41467-019-13372-2, 2019.

Hewitt, H. T., Copsey, D., Culverwell, I. D., Harris, C. M., Hill, R. S. R., Keen, A. B., McLaren, A. J., and Hunke, E. C.: Design and implementation of the infrastructure of HadGEM3: the next-generation Met Office climate modelling system, Geosci. Model Develop., 4, 223–253, https://doi.org/10.5194/gmd-4-223-2011, 2011.

Hinds, W. C.: Aerosol Technology, A Wiley-Interscience publication, second edn., ISBN:0-471-19410-7, 1998.

Inness, A., Baier, F., Benedetti, A., Bouarar, I., Chabrillat, S., Clark, H., Clerbaux, C., Coheur, P., Engelen, R. J., Errera, Q., Flemming, J., George, M., Granier, C., Hadji-Lazaro, J., Huijnen, V., Hurtmans, D., Jones, L., Kaiser, J. W., Kapsomenakis, J., Lefever, K., Leitão, J., Razinger, M., Richter, A., Schultz, M. G., Simmons, A. J., Suttie, M., Stein, O., Thépaut, J.-N., Thouret, V., Vrekoussis, M., Zerefos, C., and the MACC team: The MACC reanalysis: an 8 yr data set of atmospheric composition, Atmospheric Chemistry and Physics, 13, 4073–4109, https://doi.org/10.5194/acp-13-4073-2013, 2013.

Inness, A., Ades, M., Agustí-Panareda, A., Barré, J., Benedictow, A., Blechschmidt, A.-M., Dominguez, J. J., Engelen, R., Eskes, H., Flemming, J., Huijnen, V., Jones, L., Kipling, Z., Massart, S., Parrington, M., Peuch, V.-H., Razinger, M., Remy, S., Schulz, M., and Suttie, M.: CAMS global reanalysis (EAC4). Copernicus Atmosphere Monitoring Service (CAMS) Atmosphere Data Store (ADS), https://ads.atmosphere.copernicus.eu/cdsapp#!/dataset/cams-global-reanalysis-eac4?tab=overview, (Accessed on 11-10-2022), 2019a.

Inness, A., Ades, M., Agustí-Panareda, A., Barré, J., Benedictow, A., Blechschmidt, A.-M., Dominguez, J. J., Engelen, R., Eskes, H., Flemming, J., Huijnen, V., Jones, L., Kipling, Z., Massart, S., Parrington, M., Peuch, V.-H., Razinger, M., Remy, S., Schulz, M., and Suttie, M.: The CAMS reanalysis of atmospheric composition, Atmos. Chem. Phys., 19, 3515–3556, https://doi.org/10.5194/acp-19-3515-2019, 2019b.

Jia, H., Ma, X., Yu, F., and Quaas, J.: Significant underestimation of radiative forcing by aerosol-cloud interactions derived from satellite-based methods, Nature Comm., 12, 3649, https://doi.org/10.1038/s41467-021-23888-1, 2021.

Jia, H., Quaas, J., Gryspeerdt, E., Böhm, C., and Sourdeval, O.: Addressing the difficulties in quantifying droplet number response to aerosol from satellite observations, Atmos. Chem. Phys., 22, 7353–7372, https://doi.org/10.5194/acp-22-7353-2022, 2022.

Kaiser, J. W., Heil, A., Andreae, M. O., Benedetti, A., Chubarova, N., Jones, L., Morcrette, J.-J., Razinger, M., Schultz, M. G., Suttie, M., and van der Werf, G. R.: Biomass burning emissions estimated with a global fire assimilation system based on observed fire radiative power, Biogeosciences, 9, 527–554, https://doi.org/10.5194/bg-9-527-2012, 2012.

Kapsomenakis, J., Zerefos, C., Langerock, B., Errera, Q., Basart, S., Cuevas, E., Bennouna, Y., Thouret, V., Arola, A., Pitkänen, M., Blechschmidt, A.-M., Richter, A., Eskes, H., Tsikerdekis, T., Benedictow, A., Schulz, M., Bouarar, I., and Warneke, T.: Validation report of the CAMS global Reanalysis of aerosols and reactive gases, years 2003-2021, Copernicus Atmosphere Monitoring Service (CAMS) report, https://doi.org/10.24380/g18s-zdi, 2022.

Kapustin, V. N., Clarke, A. D., Shinozuka, Y., Howell, S., Brekhovskikh, V., Nakajima, T., and Higurashi, A.: On the determination of a cloud condensation nuclei from satellite: Challenges and possibilities, J. Geophys. Res., 111, https://doi.org/10.1029/2004JD005527, 2006.

Karydis, V. A., Kumar, P., Barahona, D., Sokolik, I. N., and Nenes, A.: On the effect of dust particles on global cloud condensation nuclei and cloud droplet number, J. Geophys. Res., 116, https://doi.org/10.1029/2011JD016283, D23204, 2011.

Kaufman, Y. J., Koren, I., Remer, L. A., Tanré, D., Ginoux, P., and Fan, S.: Dust transport and deposition observed from the Terra-Moderate Resolution Imaging Spectroradiometer (MODIS) spacecraft over the Atlantic Ocean, J. Geophys. Res., 110, https://doi.org/10.1029/2003JD004436, D10S12, 2005.

Khvorostyanov, V. I. and Curry, J. A.: Aerosol size spectra and CCN activity spectra: Reconciling the lognormal, algebraic, and power laws, J. Geophys. Res., 111, https://doi.org/10.1029/2005JD006532, 2006.

Kinne, S., O'Donnel, D., Stier, P., Kloster, S., Zhang, K., Schmidt, H., Rast, S., Giorgetta, M., Eck, T. F., and Stevens, B.: MAC-v1: A new global aerosol climatology for climate studies, J. Adv. Model. Earth Systems, 5, 704–740, https://doi.org/10.1002/jame.20035, 2013.

Köhler, H.: The nucleus in and the growth of hygroscopic droplets, Trans. Faraday Soc., 32, 1152–1161, https://doi.org/10.1039/TF9363201152, 1936.

Koren, I., Dagan, G., and Altaratz, O.: From aerosol-limited to invigoration of warm convective clouds, Science, 344, 1143–1146, https://doi.org/10.1126/science.1252595, 2014.

Kreidenweis, S. M., Petters, M., and Lohmann, U.: 100 Years of Progress in Cloud Physics, Aerosols, and Aerosol Chemistry Research, Meteorological Monographs, 59, 11.1 – 11.72, https://doi.org/https://doi.org/10.1175/AMSMONOGRAPHS-D-18-0024.1, 2019.

Lance, S., Medina, J., Smith, J., and Nenes, A.: Mapping the operation of the DMT continuous flow CCN counter, Aerosol Sci. Tech., 40, 242–254, https://doi.org/10.1080/02786820500543290, 2006.

Levy, R. C., Mattoo, S., Munchak, L. A., Remer, L. A., Sayer, A. M., Patadia, F., and Hsu, N. C.: The Collection 6 MODIS aerosol products over land and ocean, Atm. Measurem. Tech., 6, 2989–3034, https://doi.org/10.5194/amt-6-2989-2013, 2013.

Levy, R. C., Mattoo, S., Sawyer, V., Shi, Y., Colarco, P. R., Lyapustin, A. I., Wang, Y., and Remer, L. A.: Exploring systematic offsets between aerosol products from the two MODIS sensors, Atm. Measurem. Tech., 11, 4073–4092, https://doi.org/10.5194/amt-11-4073-2018, 2018.

Liu, J. and Li, Z.: Estimation of cloud condensation nuclei concentration from aerosol optical quantities: influential factors and uncertainties, Atmos. Chem. Phys., 14, 471–483, https://doi.org/10.5194/acp-14-471-2014, 2014.

Logan, T., Xi, B., and Dong, X.: Aerosol properties and their influences on marine boundary layer cloud condensation nuclei at the ARM mobile facility over the Azores, J. Geophys. Res., 119, 4859–4872, https://doi.org/10.1002/2013JD021288, 2013JD021288, 2014.

Lowe, S., Partridge, D. G., Topping, D., and Stier, P.: Inverse modelling of Köhler theory – Part 1: A response surface analysis of CCN spectra with respect to surface-active organic species, Atmospheric Chemistry and Physics, 16, 10 941–10 963, https://doi.org/10.5194/acp-16-10941-2016, 2016.

Malavelle, F., Haywood, J., A., J., Gettelman, A. C. L. B. S., R., A., I., K., J., K., L., O., , Nayeong Cho, N., Lee, D., Bellouin, N., Olivier Boucher, O., Grosvenor, D., Carslaw, K., Dhomse, S., Mann, G., Schmidt, A. and Coe, H., Hartley, M., Dalvi, M., Hill, A., Johnson, B., Johnson, C., Knight, J., O'Connor, F., Partridge, D., Stier, P., Myhre, G., Platnick, S., Stephens, G., Takahashi, H., and Thordarson, T.: Strong constraints on aerosol–cloud interactions from volcanic eruptions, Nature, 565, 485–491, https://doi.org/10.1038/nature22974, 2017.

Mangold, A., De Backer, H., De Paepe, B., Dewitte, S., Chiapello, I., Derimian, Y., Kacenelenbogen, M., Léon, J.-F., Huneeus, N., Schulz, M., Ceburnis, D., O'Dowd, C., Flentje, H., Kinne, S., Benedetti, A., Morcrette, J.-J., and Boucher, O.: Aerosol analysis and forecast in the European Centre for Medium-Range Weather Forecasts Integrated Forecast System: 3. Evaluation by means of case studies, J. Geophys. Res., 116, https://doi.org/10.1029/2010JD014864, D03302, 2011.

Mann, G. W., Carslaw, K. S., Spracklen, D. V., Ridley, D. A., Manktelow, P. T., Chipperfield, M. P., Pickering, S. J., and Johnson, C. E.: Description and evaluation of GLOMAP-mode: a modal global aerosol microphysics model for the UKCA composition-climate model, Geosci. Model Develop., 3, https://doi.org/10.5194/gmd-3-519-2010, 2010.

Morcrette, J.-J., Boucher, O., Jones, L., Salmond, D., Bechtold, P., Beljaars, A., Benedetti, A., Bonet, A., Kaiser, J. W., Razinger, M., Schulz, M., Serrar, S., Simmons, A. J., Sofiev, M., Suttie, M., Tompkins, A. M., and Untch, A.: Aerosol analysis and forecast in the European Centre for Medium-Range Weather Forecasts Integrated Forecast System: Forward modeling, J. Geophys. Res., 114, https://doi.org/10.1029/2008JD011235, D06206, 2009.

Nakajima, T., Higurashi, A., Kawamoto, K., and Penner, J. E.: A possible correlation between satellite-derived cloud and aerosol microphysical parameters, Geophys. Res. Lett., 28, 1171–1174, https://doi.org/10.1029/2000GL012186, 2001.

O'Connor, F. M., Johnson, C. E., Morgenstern, O., Abraham, N. L., Braesicke, P., Dalvi, M., Folberth, G. A., Sanderson, M. G., Telford, P. J., Voulgarakis, A., Young, P. J., Zeng, G., Collins, W. J., and Pyle, J. A.: Evaluation of the new UKCA climate-composition model - Part 2: The Troposphere, Geosci. Model Develop., 7, 41–91, https://doi.org/10.5194/gmd-7-41-2014, 2014.

Paramonov, M., Kerminen, V.-M., Gysel, M., Aalto, P. P., Andreae, M. O., Asmi, E., Baltensperger, U., Bougiatioti, A., Brus, D., Frank, G. P., Good, N., Gunthe, S. S., Hao, L., Irwin, M., Jaatinen, A., Jurányi, Z., King, S. M., Kortelainen, A., Kristensson, A., Lihavainen, H., Kulmala, M., Lohmann, U., Martin, S. T., McFiggans, G., Mihalopoulos, N., Nenes, A., O'Dowd, C. D., Ovadnevaite, J., Petäjä, T., Pöschl, U., Roberts, G. C., Rose, D., Svenningsson, B., Swietlicki, E., Weingartner, E., Whitehead, J., Wiedensohler, A., Wittbom, C., and Sierau, B.: A synthesis of cloud condensation nuclei counter (CCNC) measurements within the EUCAARI network, Atmos. Chem. Phys., 15, 12 211–12 229, https://doi.org/10.5194/acp-15-12211-2015, 2015.

Petters, M. D. and Kreidenweis, S. M.: A single parameter representation of hygroscopic growth and cloud condensation nucleus activity, Atmos. Chem. Phys., 7, 1961–1971, https://doi.org/10.5194/acp-7-1961-2007, 2007.

Pöhlker, M., Pöhlker, C., Quuas, J., Mülmenstädt, J., Pozzer, A., Andreae, M., Artaxo, P., Block, K., Coe, H., Ervens, B., Gallimore, P., Gaston, C., Gunthe, S., Henning, S., Herrmann, H., Krüger, O., McFiggans, G., Poulain, L., Raj, S., Reyes-Villegas, E., Royer, H., Walter, D., Wang, Y., and Pöschl, U.: Global organic and inorganic aerosol hygroscopicity and its effect on radiative forcing, Atmos. Chem. Phys., submitted, 2023.

Popp, T., De Leeuw, G., Bingen, C., Brühl, C., Capelle, V., Chedin, A., Clarisse, L., Dubovik, O., Grainger, R., Griesfeller, J., Heckel, A., Kinne, S., Klüser, L., Kosmale, M., Kolmonen, P., Lelli, L., Litvinov, P., Mei, L., North, P., Pinnock, S., Povey, A., Robert, C., Schulz, M., Sogacheva, L., Stebel, K., Stein Zweers, D., Thomas, G., Tilstra, L., Vandenbussche, S., Veefkind, P., Vountas, M., and Xue, Y.: Development, Production and Evaluation of Aerosol Climate Data Records from European Satellite Observations ($\text{Aerosol}_{\text{cci}}$), Rem. Sens., 8, https://doi.org/10.3390/rs8050421, 2016.

Pruppacher, H. R. and Klett, J. D.: Microphysics of Clouds and Precipitation, Kluwer Academic Publishers, second edn., ISBN:0-7923-4409-X, 1997.

Putaud, J.-P., Raes, F., Van Dingenen, R., Brüggemann, E., Facchini, M.-C., Decesari, S., Fuzzi, S., Gehrig, R., Hüglin, C., Laj, P., Lorbeer, G., Maenhaut, W., Mihalopoulos, N., Müller, K., Querol, X., Rodriguez, S., Schneider, J., Spindler, G., Brink, H., Tørseth, K., and Wiedensohler, A.: A European aerosol phenomenology - 2: chemical characteristics of particulate matter at kerbside, urban, rural and background sites in Europe, Atmos. Env., 38, 2579–2595, https://doi.org/10.1016/j.atmosenv.2004.01.041, 2004.

Putaud, J.-P., Dingenen, R. V., Alastuey, A., Bauer, H., Birmili, W., Cyrys, J., Flentje, H., Fuzzi, S., Gehrig, R., Hansson, H., Harrison, R., Herrmann, H., Hitzenberger, R., Hüglin, C., Jones, A., Kasper-Giebl, A., Kiss, G., Kousa, A., Kuhlbusch, T., Löschau, G., Maenhaut, W., Molnar, A., Moreno, T., Pekkanen, J., Perrino, C., Pitz, M., Puxbaum, H., Querol, X., Rodriguez, S., Salma, I., Schwarz, J., Smolik, J., Schneider, J., Spindler, G., Brink, H., Tursic, J., Viana, M., Wiedensohler, A., and Raes, F.: A European aerosol phenomenology - 3: Physical and chemical characteristics of particulate matter from 60 rural, urban, and kerbside sites across Europe, Atmos. Env., 44, 1308–1320, https://doi.org/10.1016/j.atmosenv.2009.12.011, 2010.

Quaas, J., Boucher, O., Bellouin, N., and Kinne, S.: Satellite-based estimate of the direct and indirect aerosol climate forcing, J. Geophys. Res., 113, https://doi.org/10.1029/2007JD008962, 2008.

Quaas, J., Ming, Y., Menon, S., Takemura, T., Wang, M., Penner, J. E., Gettelman, A., Lohmann, U., Bellouin, N., Boucher, O., Sayer, A. M., Thomas, G. E., McComiskey, A., Feingold, G., Hoose, C., Kristjánsson, J. E., Liu, X., Balkanski, Y., Donner, L. J., Ginoux, P. A., Stier, P., Grandey, B., Feichter, J., Sednev, I., Bauer, S. E., Koch, D., Grainger, R. G., Kirkevåg, A., Iversen, T., Seland, Ø., Easter, R., Ghan, S. J., Rasch, P. J., Morrison, H., Lamarque, J.-F., Iacono, M. J., Kinne, S., and Schulz, M.: Aerosol indirect effects - general circulation model intercomparison and evaluation with satellite data, Atmos. Chem. Phys., 9, 8697–8717, https://doi.org/10.5194/acp-9-8697-2009, 2009.

Quaas, J., Arola, A., Cairns, B., Christensen, M., Deneke, H., Ekman, A. M. L., Feingold, G., Fridlind, A., Gryspeerdt, E., Hasekamp, O., Li, Z., Lipponen, A., Ma, P.-L., Mülmenstädt, J., Nenes, A., Penner, J., Rosenfeld, D., Schrödner, R., Sinclair, K., Sourdeval, O., Stier, P.,

Tesche, M., van Diedenhoven, B., and Wendisch, M.: Constraining the Twomey effect from satellite observations: Issues and perspectives, Atmos. Chem. Phys., 20, 15 079–15 099, https://doi.org/10.5194/acp-20-15079-2020, 2020.

Quaas, J., Jia, H., Smith, C., Albright, A. L., Aas, W., Bellouin, N., Boucher, O., Doutriaux-Boucher, M., Forster, P. M., Grosvenor, D., Jenkins, S., Klimont, Z., Loeb, N. G., Ma, X., Naik, V., Paulot, F., Stier, P., Wild, M., Myhre, G., and Schulz, M.: Robust evidence for reversal of the trend in aerosol effective climate forcing, Atmospheric Chemistry and Physics, 22, 12 221–12 239, https://doi.org/10.5194/acp-22-12221-2022, 2022.

Reddy, M. S., Boucher, O., Bellouin, N., Schulz, M., Balkanski, Y., Dufresne, J.-L., and Pham, M.: Estimates of global multicomponent aerosol optical depth and direct radiative perturbation in the Laboratoire de Meteorologie Dynamique general circulation model, J. Geophys. Res., 110, https://doi.org/10.1029/2004JD004757, 2005.

Remer, L., Kaufman, Y. J., Tanre, D., Mattoo, S., Chu, D. A., Martins, J. V., Li, R.-R., Ichoku, C., Levy, R. C., Kleidman, R. G., Eck, T. F., Vermote, E., and Holben, B. N.: The MODIS Aerosol Algorithm, Products, and Validation, J. Atmos. Sci., 62, 947–973, https://doi.org/10.1175/JAS3385.1, 2005.

Rémy, S., Kipling, Z., Flemming, J., Boucher, O., Nabat, P., Michou, M., Bozzo, A., Ades, M., Huijnen, V., Benedetti, A., Engelen, R., Peuch, V.-H., and Morcrette, J.-J.: Description and evaluation of the tropospheric aerosol scheme in the European Centre for Medium-Range Weather Forecasts (ECMWF) Integrated Forecasting System (IFS-AER, cycle 45R1), Geosci. Model Develop., 12, 4627–4659, https://doi.org/10.5194/gmd-12-4627-2019, 2019.

Roberts, G. and Nenes, A.: A continuous-flow streamwise thermal-gradient CCN chamber for atmospheric measurements, Aerosol Sci. Tech., 39, 206–221, https://doi.org/10.1080/027868290913988, 2005.

Rose, D., Gunthe, S., Mikhailov, E., Frank, G., Dusek, U., Andreae, M., and Pöschl, U.: Calibration and measurement uncertainties of a continuous-flow cloud condensation nuclei counter (DMT-CCNC): CCN activation of ammonium sulfate and sodium chloride aerosol particles in theory and experiment, Atmos. Chem. Phys., 8, 1153–1179, https://doi.org/doi:10.5194/acp-8-1153-2008, 2008.

Schmale, J., Henning, S., Henzing, B., Keskinen, H., Sellegri, K., Ovadnevaite, J., Bougiatioti, A., Kalivitis, N., Stavroulas, I., Jefferson, A., Park, M., Schlag, P., Kristensson, A., Iwamoto, Y., Pringle, K., Reddington, C., Aalto, P., Äijälä, M., Baltensperger, U., Bialek, J., Birmili, W., Bukowiecki, N., Ehn, M., Fjæraa, A., Fiebig, M., Frank, G., Fröhlich, R., Frumau, A., Furuya, M., Hammer, E., Heikkinen, L., Herrmann, E., Holzinger, R., Hyono, H., Kanakidou, M., Kiendler-Scharr, A., Kinouchi, K., Kos, G., Kulmala, M., Mihalopoulos, N., Motos, G., Nenes, A., O'Dowd, C., Paramonov, M., Petäjä, T., Picard, D., Poulain, L., Prévôt, A., Slowik, J., Sonntag, A., Swietlicki, E., Svenningsson, B., Tsurumaru, H., Wiedensohler, A., Wittbom, C., Ogren, J., Matsuki, A., Yum, S., Myhre, C., Carslaw, K., Stratmann, F., and Gysel, M.: Collocated observations of cloud condensation nuclei, particle size distributions, and chemical composition, Scientific Data, 4, https://doi.org/10.1038/sdata.2017.3, 2017.

Schmale, J., Henning, S., Decesari, S., Henzing, B., Keskinen, H., Sellegri, K., Ovadnevaite, J., Pöhlker, M. L., Brito, J., Bougiatioti, A., Kristensson, A., Kalivitis, N., Stavroulas, I., Carbone, S., Jefferson, A., Park, M., Schlag, P., Iwamoto, Y., Aalto, P., Äijälä, M., Bukowiecki, N., Ehn, M., Frank, G., Fröhlich, R., Frumau, A., Herrmann, E., Herrmann, H., Holzinger, R., Kos, G., Kulmala, M., Mihalopoulos, N., Nenes, A., O'Dowd, C., Petäjä, T., Picard, D., Pöhlker, C., Pöschl, U., Poulain, L., Prévôt, A. S. H., Swietlicki, E., Andreae, M. O., Artaxo, P., Wiedensohler, A., Ogren, J., Matsuki, A., Yum, S. S., Stratmann, F., Baltensperger, U., and Gysel, M.: Long-term cloud condensation nuclei number concentration, particle number size distribution and chemical composition measurements at regionally representative observatories, Atmos. Chem. Phys., 18, 2853–2881, https://doi.org/10.5194/acp-18-2853-2018, 2018.

Seinfeld, J. H. and Pandis, S. N.: Atmospheric Chemistry and Physics - From Air Pollution to Climate Change, A Wiley-Interscience publication, second edn., ISBN:978-0-471-72018-8, 2006.

Shi, Y., Flynn, C., and Jefferson, A.: Aerosol Observing System Cloud Condensation Nuclei Average (AOSCCNAVG) Value-Added Product, Tech. Rep. DOE/SC-ARM/TR-130, U.S. Department of Energy, http://www.arm.gov/publications/tech_reports/doe-sc-arm-tr-130.pdf?id=72, 2013.

Shinozuka, Y., Clarke, A. D., Nenes, A., Jefferson, A., Wood, R., McNaughton, C. S., Ström, J., Tunved, P., Redemann, J., Thornhill, K. L., Moore, R. H., Lathem, T. L., Lin, J. J., and Yoon, Y. J.: The relationship between cloud condensation nuclei (CCN) concentration and light extinction of dried particles: indications of underlying aerosol processes and implications for satellite-based CCN estimates, Atmos. Chem. Phys., 15, 7585–7604, https://doi.org/10.5194/acp-15-7585-2015, 2015.

Sindelarova, K., Granier, C., Bouarar, I., Guenther, A., Tilmes, S., Stavrakou, T., Müller, J.-F., Kuhn, U., Stefani, P., and Knorr, W.: Global data set of biogenic VOC emissions calculated by the MEGAN model over the last 30 years, Atmos. Chem. Phys., 14, 9317–9341, https://doi.org/10.5194/acp-14-9317-2014, 2014.

Spracklen, D. V., Pringle, K. J., Carslaw, K. S., Chipperfield, M. P., and Mann, G. W.: A global off-line model of size-resolved aerosol microphysics: I. Model development and prediction of aerosol properties, Atmos. Chem. Phys., 5, 2227–2252, https://doi.org/10.5194/acp-5-2227-2005, 2005.

Spracklen, D. V., Carslaw, K. S., Pöschl, U., Rap, A., and Forster, P. M.: Global cloud condensation nuclei influenced by carbonaceous combustion aerosol, Atmos. Chem. Phys., 11, 9067–9087, https://doi.org/10.5194/acp-11-9067-2011, 2011.

Stein, O., Schultz, M. G., Bouarar, I., Clark, H., Huijnen, V., Gaudel, A., George, M., and Clerbaux, C.: On the wintertime low bias of Northern Hemisphere carbon monoxide found in global model simulations, Atmos. Chem. Phys., 14, 9295–9316, https://doi.org/10.5194/acp-14-9295-2014, 2014.

Stevens, B., Giorgetta, M., Esch, M., Mauritsen, T., Crueger, T., Rast, S., Salzmann, M., Schmidt, H., Bader, J., Block, K., Brokopf, R., Fast, I., Kinne, S., Kornblueh, L., Lohmann, U., Pincus, R., Reichler, T., and Roeckner, E.: Atmospheric component of the MPI-M Earth System Model: ECHAM6, J. Adv. Model. Earth Systems, 5, 146–172, https://doi.org/10.1002/jame.20015, 2013.

Stier, P.: Limitations of passive remote sensing to constrain global cloud condensation nuclei, Atmos. Chem. Phys., 16, 6595–6607, https://doi.org/10.5194/acp-16-6595-2016, 2016.

Stier, P., Feichter, J., Kinne, S., Kloster, S., Vignati, E., Wilson, J., Ganzeveld, L., Tegen, I., Werner, M., Balkanski, Y., Schulz, M., Boucher, O., Minikin, A., and Petzold, A.: The aerosol-climate model ECHAM5-HAM, Atmos. Chem. Phys., 5, 1125–1156, https://doi.org/10.5194/acp-5-1125-2005, 2005.

Szopa, S., Naik, V., Adhikary, B., Artaxo, P., Berntsen, T., Collins, W., Fuzzi, S., Gallardo, L., Kiendler-Scharr, A., Klimont, Z., Liao, H., Unger, N., and Zanis, P.: Short-Lived Climate Forcers, in: Climate Change 2021: The Physical Science Basis. Contribution of Working Group I to the Sixth Assessment Report of the Intergovernmental Panel on Climate Change, edited by Masson-Delmotte, V., Zhai, P., Pirani, A., Connors, S., Péan, C., Berger, S., Caud, N., Chen, Y., Goldfarb, L., Gomis, M., Huang, M., Leitzell, K., Lonnoy, E., Matthews, J., Maycock, T., Waterfield, T., Yelekçi, O., Yu, R., and Zhou, B., p. 817–922, Cambridge University Press, Cambridge, United Kingdom and New York, NY, USA, https://doi.org/10.1017/9781009157896.008, 2021.

Twomey, S.: The nuclei of natural cloud formation part II: The supersaturation in natural clouds and the variation of cloud droplet concentration, Pure and Appl. Geophys., 43, 243–249, https://doi.org/10.1007/BF01993560, 1959.

Van Dingenen, R., Raes, F., Putaud, J.-P., Baltensperger, U., Charron, A., Facchini, M.-C., Decesari, S., Fuzzi, S., Gehrig, R., Hansson, H.-C., Harrison, R. M., Hüglin, C., Jones, A. M., Laj, P., Lorbeer, G., Maenhaut, W., Palmgren, F., Querol, X., Rodriguez, S., Schneider, J., Brink, H., Tunved, P., Tørseth, K., Wehner, B., Weingartner, E., Wiedensohler, A., and Wåhlin, P.: A European aerosol phenomenology

- 1: physical characteristics of particulate matter at kerbside, urban, rural and background sites in Europe, Atmos. Env., 38, 2561–2577, https://doi.org/10.1016/j.atmosenv.2004.01.040, 2004.

Vignati, E., Wilson, J., and Stier, P.: M7: An efficient size-resolved aerosol microphysics module for large-scale aerosol transport models, J. Geophys. Res., 109, https://doi.org/10.1029/2003JD004485, 2004.

Watson-Parris, D., Schutgens, N., Reddington, C., Pringle, K. J., Liu, D., Allan, J. D., Coe, H., Carslaw, K. S., and Stier, P.: In situ constraints on the vertical distribution of global aerosol, Atmospheric Chemistry and Physics, 19, 11 765–11 790, https://doi.org/10.5194/acp-19-11765-2019, 2019.

West, R. E. L., Stier, P., Jones, A., Johnson, C. E., Mann, G. W., Bellouin, N., Partridge, D. G., and Kipling, Z.: The importance of vertical velocity variability for estimates of the indirect aerosol effects, Atmos. Chem. Phys., 14, 6369–6393, https://doi.org/10.5194/acp-14-6369-2014, 2014.

Winker, D. M., Tackett, J. L., Getzewich, B. J., Liu, Z., Vaughan, M. A., and Rogers, R. R.: The global 3-D distribution of tropospheric aerosols as characterized by CALIOP, Atmos. Chem. Phys., 13, 3345–3361, https://doi.org/10.5194/acp-13-3345-2013, 2013.

Wood, R., Stemmler, J. D., Rémillard, J., and Jefferson, A.: Low-CCN concentration air masses over the eastern North Atlantic: Seasonality, meteorology, and drivers, J. Geophys. Res., 122, 1203–1223, https://doi.org/https://doi.org/10.1002/2016JD025557, 2017.

Zhang, J. and Reid, J. S.: MODIS aerosol product analysis for data assimilation: Assessment of over-ocean level 2 aerosol optical thickness retrievals, J. Geophys. Res., 111, https://doi.org/10.1029/2005JD006898, 2006.

Zhang, K., O'Donnell, D., Kazil, J., Stier, P., Kinne, S., Lohmann, U., Ferrachat, S., Croft, B., Quaas, J., Wan, H., Rast, S., and Feichter, J.: The global aerosol-climate model ECHAM-HAM, version 2: sensitivity to improvements in process representations, Atmos. Chem. Phys., 12, 8911–8949, https://doi.org/10.5194/acp-12-8911-2012, 2012.

Zieger, P., Väisänen, O., Corbin, J., Partridge, D., Bastelberger, S., Mousavi-Fard, M., Rosati, B., Gyse, M., Krieger, U., Leck, C., Nenes, A., Piipinen, I., Virtanen, A., and Salter, M.: Revising the hygroscopicity of inorganic sea salt particles, Nature Comm., 8, https://doi.org/10.1038/ncomms15883, 2017.